Dual-Functional Radar-Communication Waveform Design: A Symbol-Level Precoding Approach

Rang Liu, *Graduate Student Member, IEEE*, Ming Li, *Senior Member, IEEE*, Qian Liu, *Member, IEEE*, and A. Lee Swindlehurst, *Fellow, IEEE*

***Abstract*—Dual-functional radar-communication (DFRC) systems can simultaneously perform both radar and communication functionalities using the same hardware platform and spectrum resource. In this paper, we consider multi-input multi-output (MIMO) DFRC systems and focus on transmit beamforming designs to provide both radar sensing and multi-user communications. Unlike conventional block-level precoding techniques, we propose to use the recently emerged symbol-level precoding approach in DFRC systems, which provides additional degrees of freedom (DoFs) that guarantee preferable instantaneous transmit beampatterns for radar sensing and achieve better communication performance. In particular, the squared error between the designed and desired beampatterns is minimized subject to the quality-of-service (QoS) requirements of the communication users and the constant-modulus power constraint. Two efficient algorithms are developed to solve this non-convex problem on both the Euclidean and Riemannian spaces. The first algorithm employs penalty dual decomposition (PDD), majorization-minimization (MM), and block coordinate descent (BCD) methods to convert the original optimization problem into two solvable sub-problems, and iteratively solves them using efficient algorithms. The second algorithm provides a much faster solution at the price of a slight performance loss, first transforming the original problem into Riemannian space, and then utilizing the augmented Lagrangian method (ALM) to obtain an unconstrained problem that is subsequently solved via a Riemannian Broyden-Fletcher-Goldfarb-Shanno (RBFGS) algorithm. Extensive simulations verify the distinct advantages of the proposed symbol-level precoding designs in both radar sensing and multi-user communications.**

***Index Terms*—Dual-functional radar-communication (DFRC), multi-input multi-output (MIMO), symbol-level precoding, radar sensing, multi-user communications.**

Manuscript received January 30, 2021; revised June 19, 2021 and August 29, 2021; accepted September 1, 2021. Date of publication September 9, 2021; date of current version December 2, 2021. This work was supported in part by the National Natural Science Foundation of China under Grants 61971088, 62071083, U1808206, and U1908214, in part by the Natural Science Foundation of Liaoning Province under Grant 2020-MS-108, in part by the Fundamental Research Funds for the Central Universities under Grant DUT20GJ214, and in part by Dalian Science and Technology Innovation Project under Grant 2020JJ25CY001. The work of A. L. Swindlehurst was supported in part by the U.S. National Science Foundation under Grant CCF-2008714. The guest editor coordinating the review of this manuscript and approving it for publication was Prof. J. Andrew Zhang. *(Corresponding author: Ming Li.)*

Rang Liu and Ming Li are with the School of Information and Communication Engineering, Dalian University of Technology, Dalian 116024, China (e-mail: liurang@mail.dlut.edu.cn; mli@dlut.edu.cn).

Qian Liu is with the School of Computer Science and Technology, Dalian University of Technology, Dalian 116024, China (e-mail: qianliu@dlut.edu.cn).

A. Lee Swindlehurst is with the Center for Pervasive Communications and Computing, University of California, Irvine, CA 92697 USA (e-mail: swindle@uci.edu).

Digital Object Identifier 10.1109/JSTSP.2021.3111438

I. Introduction

SPECTRUM sharing has been regarded as a promising solution for tackling the spectrum congestion problem in rapidly expanding wireless communication networks. One of the most popular examples is spectrum sharing between radar and wireless communication systems, which has been widely investigated from theoretical performance analyses to practical waveform designs [1]–[3]. Previous work on joint radar-communication design mainly focuses on: 1) Radar-Communication Coexistence (RCC) and 2) Dual-Functional Radar-Communication (DFRC) designs. In RCC systems, non-colocated radar and communication systems must exchange necessary side-information for performing interference management and achieving better cooperation [4], [5], which greatly increases the system complexity and cost. On the other hand, DFRC systems simultaneously perform both radar and communication functionalities using the same signals transmitted from a fully-shared transmitter, which only requires one smaller-size, lower-cost, and lower-complexity platform and naturally achieves full cooperation. Therefore, DFRC systems have a competitive advantage and many novel applications have been proposed in recent years [6].

In DFRC systems, the radar and communication functionalities inherently have conflicting requirements in terms of, e.g., the antenna placement, the operation region of the power-amplifiers, the signal formats, etc. Therefore, the transmit waveform should be carefully designed to balance the requirements of these two functionalities and achieve better system performance. In addition, multi-input multi-output (MIMO) architectures are also widely applied in DFRC systems to provide waveform diversity for radar target detection [7], and beamforming gains and spatial multiplexing for multi-user communications.

The existing research on waveform design for DFRC systems can be divided into two main categories: radar-centric and communication-centric approaches. The radar-centric approach prioritizes radar sensing functionality and realizes communication by embedding information symbols into the radar waveform [8], [9], which permits only a very low transmission rate since only limited symbols can be embedded into each radar pulse. Furthermore, considering security and cost, government and military agencies usually do not allow changes to their radar systems [6]. Thus the communication-centric approach, which typically relies on transmit beamforming from multi-antenna base stations (BSs) to support radar sensing, is more attractive and more widely considered.

Recently, many researchers have devoted themselves to transmit beamforming designs in MIMO DFRC systems [10]–[20], where the precoding matrix is optimized with different radar sensing and communication metrics. Typical radar sensing

metrics include the radar receiver's signal-to-interference-plus-noise ratio (SINR) [11], the beampattern mean squared error (MSE) [12], the Cramér-Rao bound [13], and the similarity between the designed beamformer and that of the reference radar-only system [14]–[17]. Meanwhile, widely-used communication metrics include the achievable rate [18], [19], the communication user's SINR [14], [16], [20], and the multi-user interference (MUI) [12], [15]. The combination of radar sensing and communication metrics can provide a comprehensive criteria for evaluating the performance of DFRC systems [12]–[15].

In the transmit waveform designs mentioned above [10]–[20], conventional linear block-level precoding is used to embed the communication symbols into the dual-function transmit waveform. The available degrees of freedom (DoFs) of these approaches have been proven to be limited by the number of users [21]. In order to increase the number of DoFs in the transmit waveform for better radar sensing performance, the authors in [21]–[23] proposed to transmit both the precoded communication symbols and the radar waveform, which are jointly designed in a block-level fashion. However, such block-level precoding designs inherently have limited DoFs due to their restriction to linear processing. More importantly, since block-level precoding designs employ performance metrics based on second-order statistics (e.g., SINR and MSE) to optimize the average transmit beampattern, the radar sensing performance can be guaranteed only when the number of transmitted symbols is sufficiently large. In other words, the instantaneous transmit beampatterns in different time slots might have significant distortions, which causes severe performance degradation on target detection and parameter estimation if only a limited number of samples are collected. In light of these shortcomings for block-level precoding, more sophisticated transmit beamforming strategies are necessary to fully exploit the DoFs available for simultaneously providing reliable radar sensing and high-rate communications. This finding motivates us to employ the recently emerged symbol-level precoding approach in DFRC systems.

Symbol-level precoding has been proposed as a way of exploiting rather than simply eliminating MUI in multi-user communication systems [24]–[29]. Unlike conventional block-level precoding, symbol-level precoding is a non-linear and symbol-dependent approach, which optimizes each instantaneous transmitted vector based on the specific symbols to be transmitted. In this way, the instantaneous transmit beampattern in each time slot can be carefully designed in a symbol-by-symbol fashion, i.e., sample-by-sample in the context of radar waveforms, to provide more DoFs for radar sensing functionality. Therefore, by utilizing the symbol-level precoding (sample-level waveform) technique, a well-formed beampattern can be guaranteed with a limited number of waveform samples. From the communication perspective, instead of suppressing MUI in a statistical manner, symbol-level precoding can exploit the transmitted symbol information to convert harmful MUI into constructive components for enhancing the symbol detection performance and performing more reliable multi-user communications. Therefore, the symbol-level precoding technique, which exploits more available DoFs in both the spatial and temporal domains, can provide consistently improved instantaneous transmit beampatterns to achieve better radar sensing performance, as well as convert harmful MUI into constructive interference (CI) for improving the quality-of-service (QoS) of multi-user communications.

In prior work [5], symbol-level precoding technique has been employed in a RCC system to enjoy the advantages of interference exploitation. However, in RCC systems, the symbol-level precoding design only optimizes the communication functionality and simultaneously suppresses the interference to the radar system regardless of specific radar waveforms. On the contrary, in the considered DFRC system in this paper, the symbol-level precoding design focuses on the dual-use waveform, which simultaneously realizes both communication and radar sensing functionalities. Therefore, the symbol-level precoding design for DFRC systems is quite different from that for RCC systems, and has not been previously investigated in the literature.

In this paper, we investigate symbol-level precoding designs for a MIMO DFRC system, where a multi-antenna BS simultaneously serves multiple single-antenna communication users and detects targets from several directions of interest. In particular, the symbol-level precoded transmit vector is optimized to minimize the squared error between the obtained and desired beampatterns under the communication QoS requirements and the constant-modulus power constraint. The main contributions can be summarized as follows:

- For the first time, we employ symbol-level precoding techniques in DFRC systems to provide additional DoFs for the waveform designs, which (i) allows desirable transmit beampatterns to be realized in every time slot rather than just "on average," and (ii) significantly improves the simultaneous multi-user communication performance by converting harmful MUI into useful signals. Compared with conventional designs based on second-order statistics and block-level precoding, our symbol-level precoding approach imposes different radar sensing and multi-user communication constraints and leads to a brand-new waveform design problem.
- In order to handle the resulting complicated non-convex waveform design problem, we first develop an algorithm framework that combines penalty dual decomposition (PDD), majorization-minimization (MM), and block coordinate descent (BCD) methods to convert the problem into two solvable sub-problems. Then, a closed-form phase alignment and a Lagrangian dual approach are applied to efficiently solve these sub-problems.
- We further propose a more computationally efficient solution that results in only a slight performance loss. In this second approach, we convert the original problem into Riemannian space, and utilize the augmented Lagrangian method (ALM) to transform it into an unconstrained problem. Then, an efficient Riemannian Broyden-Fletcher-Goldfarb-Shanno (RBFGS) algorithm is developed to solve this problem.
- Finally, we provide extensive simulation results to demonstrate the distinct advantages of the proposed symbol-level precoding designs in both radar sensing and multi-user communications.

The rest of this paper is organized as follows. Section II introduces the system model, the performance metrics for multi-user communications and radar sensing, and the problem formulation. The proposed PDD-MM-BCD and ALM-RBFGS algorithms are developed in Sections III and IV, respectively. Possible extensions of the proposed approach to scenarios that require Doppler processing are described in Section V. Simulation results are presented in Section VI, and finally conclusions are provided in Section VII.

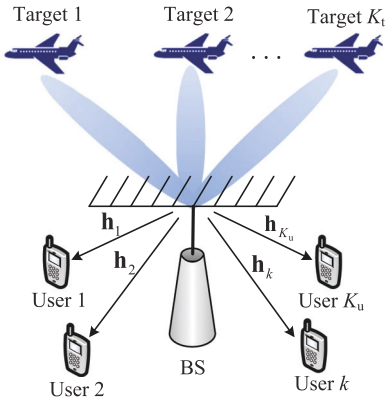

Fig. 1. A dual-functional radar-communication system.

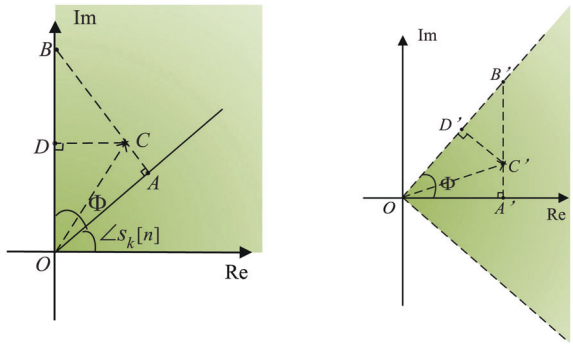

Fig. 2. Constructive region for a QPSK symbol. (a) An example of the constructive region. (b) After rotating the diagram in Fig. 2(a) clockwise.

Notation: Boldface lower-case and upper-case letters indicate column vectors and matrices, respectively. $(\cdot)^T$ and $(\cdot)^H$ denote the transpose and the transpose-conjugate operations, respectively. $\mathbb{C}$ denotes the set of complex numbers. $|a|$ and $\|\mathbf{a}\|$ are the magnitude of a scalar a and the norm of a vector $\mathbf{a}$, respectively. $\angle a$ is the angle of complex-valued a. $\Re\{\cdot\}$ and $\Im\{\cdot\}$ denote the real and imaginary part of a complex number, respectively. $\odot$ denotes the Hadamard product. $\mathbf{A} \succeq \mathbf{0}$ indicates that the matrix $\mathbf{A}$ is positive semi-definite. $\mathbf{I}_M$ indicates an $M \times M$ identity matrix. Finally, we adopt the following indexing notation: $\mathbf{A}(i,j)$ denotes the element of the i-th row and the j-th column of matrix $\mathbf{A}$, and $\mathbf{a}(i)$ denotes the i-th element of vector $\mathbf{a}$.

II. System Model and Problem Formulation

A. System Model

We consider a colocated monostatic MIMO DFRC system as shown in Fig. 1, where a BS is equipped with M antennas in a uniform linear array (ULA). The BS simultaneously serves K_{u} single-antenna communication users and detects the locations of K_{t} targets. Generally, $K_{\mathrm{u}} \leq M$ and $K_{\mathrm{t}} \leq M$. The BS periodically emits short and high-power pulse-modulated signals to implement DFRC. The same antenna array is used for both transmit and receive in different time slots via time-division (TD) processing. In particular, the BS first transmits radar pulses that are embedded with communication symbols to simultaneously illuminate the targets of interest and transfer information to the communication users. Then, the BS switches to the radar receiver mode, collects the reflected echo signals from the targets, and further estimates the targets' parameters of interest based on the prior knowledge of the transmitted radar pulses and advanced estimation algorithms.

In this paper, we employ non-linear symbol-level precoding to realize both multi-target radar sensing and multi-user communications. Specially, let $\mathbf{x}[n] \triangleq [x_1[n], x_2[n], \ldots, x_M[n]]^T$ be the precoded transmit vector in the n-th time slot (symbol duration), where $x_m[n]$ is the baseband signal transmitted from the m-th antenna, $m = 1, 2, \ldots, M$. In the radar context, $\mathbf{x}[n]$ is also considered to be the n-th sample of the radar waveform. Let $\mathbf{s}[n] \triangleq [s_1[n], s_2[n], \ldots, s_{K_{\mathrm{u}}}[n]]^T$ be the symbols transmitted to the K_{u} users. Unlike conventional block-level precoding designs where $\mathbf{x}[n]$ is a linear function of $\mathbf{s}[n]$, symbol-level precoding in general employs a non-linear mapping from $\mathbf{s}[n]$ to $\mathbf{x}[n]$, and optimizes $\mathbf{x}[n]$ directly according to the instantaneous symbol vector $\mathbf{s}[n]$ instead of using second-order statistics-based metrics. Therefore, symbol-level precoding can exploit more DoFs to improve both radar sensing and multi-user communication performance, as well as guarantee superior instantaneous transmit beampatterns. Since the conventional statistical metrics, e.g., SINR and MSE, are inappropriate to evaluate the performance of the symbol-level precoding designs, we will describe the symbol-level precoding performance metrics for multi-user communications and radar sensing in the following two subsections, respectively.

B. Multi-User Communication Performance Metric

To simplify the description of our approach, in this paper we will assume that the transmitted symbols $\mathbf{s}[n]$ are independently selected from an Ω-phase-shift-keying (PSK) constellation. Modifications necessary to accommodate other modulation types, e.g., quadrature amplitude modulation (QAM), will be briefly discussed below. For transmitting $\mathbf{s}[n]$ in the n-th time slot, the symbol-level precoded transmit vector $\mathbf{x}[n]$ is designed and transmitted from the multiple antennas. The received signal at the k-th user is thus written as

$$r_k[n] = \mathbf{h}_k^H \mathbf{x}[n] + n_k[n], \tag{1}$$

where $\mathbf{h}_k \in \mathbb{C}^M$ is the Rayleigh fading channel from the BS to the k-th user, and $n_k[n] \sim \mathcal{CN}(0, \sigma_k^2)$ is the additive white Gaussian noise (AWGN) at the k-th user.

Symbol-level precoding relies on the idea of CI, in which harmful MUI is converted into helpful signals that push the received signals farther away from their decision boundaries [24]–[29]. Thus, the Euclidean distance between the received noise-free signal and its closest decision boundaries is usually adopted as the QoS metric to evaluate the communication performance since it directly determines the symbol error rate (SER). The idea is illustrated in Fig. 2 for quadrature-PSK (QPSK) signals, where the green sector is the decision region when the desired symbol is $s_k[n] = e^{j\pi/4}$, $\overrightarrow{OC} = \mathbf{h}_k^H \mathbf{x}[n]$ is the received noise-free signal at the k-th user, $\Phi = \pi/\Omega$, points A and D are the projections of point C on the direction of $s_k[n]$ and the corresponding nearest decision boundary, respectively, and point B is the intersection of the extension of $\overrightarrow{AC}$ and the nearest decision boundary. We see that $s_k[n]$ can be correctly detected at the k-th user when the received signal $r_k[n]$ lies in the green region. In order to

improve the robustness to noise, the transmitted signal $\mathbf{x}[n]$ should be designed such that the received noise-free signal $\overrightarrow{OC}$ is as far away from its decision boundaries as possible. Therefore, the minimum Euclidean distance between the received noise-free signal and its decision boundaries, i.e., $|\overrightarrow{CD}|$, is taken to be the communication QoS metric. In order to facilitate the expression of $|\overrightarrow{CD}|$, we rotate the diagram in Fig. 2(a) clockwise by $\angle s_k[n]$ degrees as shown in Fig. 2(b). Then, the distance between the received noise-free signal and its closest decision boundary can be readily expressed as

$$\begin{aligned}\left|\overrightarrow{C'D'}\right| &= \left|\overrightarrow{C'B'}\right|\cos\Phi = \left(\left|\overrightarrow{A'B'}\right| - \left|\overrightarrow{A'C'}\right|\right)\cos\Phi \\ &= \left[\Re\{\overrightarrow{OC'}\}\tan\Phi - \left|\Im\{\overrightarrow{OC'}\}\right|\right]\cos\Phi \\ &= \Re\{\mathbf{h}_k^H\mathbf{x}[n]e^{-j\angle s_k[n]}\}\sin\Phi \\ &\quad - \left|\Im\{\mathbf{h}_k^H\mathbf{x}[n]e^{-j\angle s_k[n]}\}\right|\cos\Phi. \end{aligned} \tag{2}$$

Thus, to guarantee the multi-user communication QoS, the transmitted signal $\mathbf{x}[n]$ should be designed to ensure that the distance (2) is no less than a preset minimum; i.e., the communication constraint is formulated as

$$\begin{aligned}&\Re\left\{\mathbf{h}_k^H\mathbf{x}[n]e^{-j\angle s_k[n]}\right\}\sin\Phi \\ &\quad - \left|\Im\left\{\mathbf{h}_k^H\mathbf{x}[n]e^{-j\angle s_k[n]}\right\}\right|\cos\Phi \geq \beta_k, \end{aligned} \tag{3}$$

where $\beta_k > 0$ is the preset minimum QoS requirement for the k-th user.

The approach described above is similar for other types of signal constellations; the constructive region (CR) for different constellations is just expressed by a different set of inequalities. For example, in the case of QAM, there are three different types of CRs, depending on whether the symbol is from an inner constellation point, an outer point on the corners, or an outer point on the sides. Each type of CR is a convex region that can be expressed as linear inequalities on $\Re\{\mathbf{h}_k^H\mathbf{x}[n]\}$ and $\Im\{\mathbf{h}_k^H\mathbf{x}[n]\}$. (See [30]–[32] for further details). Thus, the algorithms proposed later in this work can be easily extended to QAM and indeed arbitrary modulation formats, provided the symbol decision regions are convex.

C. Radar Sensing Performance Metric

For radar sensing purposes, the waveforms are usually designed to direct the transmit beam towards the directions of potential targets, so that they can be illuminated by stronger signals. This allows the radar receiver to obtain stronger echo signals from the targets, which yields more accurate estimation of the parameters of interest. To evaluate the transmit beampattern, in this subsection we first derive the received signal and corresponding beampattern for each direction, and then formulate the squared error between the designed and desired beampatterns as a radar sensing performance metric.

In the considered MIMO DFRC system, the symbol-level precoded transmit signal $\mathbf{x}[n]$ is also taken to be the n-th sample of the radar waveform. Moreover, narrow-band waveforms and line-of-sight (LoS) propagation are usually assumed in MIMO radar systems. Thus, the baseband signal at the angular direction $\theta \in [-\frac{\pi}{2}, \frac{\pi}{2})$ can be expressed as

$$r(n;\theta) = \mathbf{a}^H(\theta)\mathbf{x}[n], \tag{4}$$

where $\mathbf{a}(\theta) \triangleq [1, e^{j\frac{2\pi}{\lambda}\Delta\sin(\theta)}, \ldots, e^{j\frac{2\pi}{\lambda}(M-1)\Delta\sin(\theta)}]^T \in \mathbb{C}^M$ is the transmit steering vector for direction θ, with Δ representing the antenna spacing and λ the wavelength. When the transmit signal is reflected by K_t point-like targets at the directions $\theta_{k_\mathrm{t}}, k_\mathrm{t} = 1, \ldots, K_\mathrm{t}$, the received signal at the BS is written as

$$\mathbf{y}[n] = \sum_{k_\mathrm{t}=1}^{K_\mathrm{t}} \beta_{k_\mathrm{t}}\mathbf{a}(\theta_{k_\mathrm{t}})\mathbf{a}^H(\theta_{k_\mathrm{t}})\mathbf{x}[n] + \mathbf{z}[n], \tag{5}$$

where β_{k_t} is the complex amplitude proportional to the radar-cross section (RCS) of the target at the direction θ_{k_t}, and $\mathbf{z}[n] \sim \mathcal{CN}(0, \sigma_\mathrm{z}^2)$ is AWGN. In this work, we assume that the targets are stationary or very slowly-moving with Doppler frequencies near zero, and they are located in the same range bin for simplicity. Therefore, the radar sensing problem in this paper essentially focuses on estimating the RCS β_{k_t} and the angular direction θ_{k_t} for all k_t. This further implies that our problem formulation will not consider the temporal correlation properties of the transmitted waveforms. In Section V we briefly discuss some ideas for extending the approach to the case with non-negligible Doppler.

To facilitate the target detection and parameter estimation, a widely acknowledged method is to maximize the signal power in the directions of potential targets and minimize it elsewhere, in such a way to enhance the echo signals from the targets and suppress clutter. In such approaches, the transmit beampattern is optimized to approach an ideal radar beampattern. Thus, the similarity between the designed and desired transmit beampatterns is a popular radar waveform design metric [7], [33]. It is noted that in existing works [10]–[23] using conventional block-level precoding, the *average* transmit beampattern is considered in the waveform optimization:

$$P(\theta;\mathbf{R}) = \mathbb{E}\left\{\left|\mathbf{a}^H(\theta)\mathbf{x}[n]\right|^2\right\} = \mathbf{a}^H(\theta)\mathbf{R}\mathbf{a}(\theta), \tag{6}$$

where $\mathbf{R} \triangleq \mathbb{E}\{\mathbf{x}[n]\mathbf{x}[n]^H\}$ is the covariance matrix of the transmitted signals. In a block-level precoding system with precoding matrix $\mathbf{F}$ and $\mathbf{x}[n] = \mathbf{F}\mathbf{s}[n]$, the transmitted symbols are typically assumed to be statistically independent, i.e., $\mathbb{E}\{\mathbf{s}[n]\mathbf{s}[n]^H\} = \mathbf{I}_{K_\mathrm{u}}$. Thus, the design of the covariance matrix of the transmitted signals is equal to that of the precoder, i.e., $\mathbf{R} = \mathbf{F}\mathbf{F}^H$. In designing the precoder $\mathbf{F}$ to match the ideal beampattern, since the second-order statistics of the transmitted symbols are used to derive the average transmit beampattern (6), the number of transmitted signals/waveform samples must be sufficiently large to support this assumption. However, in DFRC systems, the number of waveform samples in each radar pulse is usually limited, which consequently might cause significant distortions to the actual average beampattern obtained with only a few radar pulses. This can result in severe target detection and parmeter estimation perfomance since the transmit power cannot be better focused on the directions of interest to obtain stronger reflected echoes from the targets for sensing. In order to overcome this drawback, we employ symbol-level precoding, which optimizes the *instantaneous* transmit beampattern by directly designing the transmitted signal $\mathbf{x}[n]$, and thus can provide satisfactory radar sensing performance with a limited number of samples.

With the transmitted signal $\mathbf{x}[n]$ in the n-th time slot, the instantaneous transmit beampattern (signal power) at direction θ is given by

$$P\left(\theta;\mathbf{x}[n]\right)=\left|\mathbf{a}^H(\theta)\mathbf{x}[n]\right|^2=\mathbf{x}^H[n]\mathbf{A}(\theta)\mathbf{x}[n], \tag{7}$$

where $\mathbf{A}(\theta)\triangleq\mathbf{a}(\theta)\mathbf{a}^H(\theta)$ for brevity. Then, the radar sensing performance metric, i.e., the difference between the designed instantaneous transmit beampattern $P(\theta;\mathbf{x}[n])$ and desired beampattern $d(\theta)$, is formulated in terms of squared error as

$$f\left(\alpha,\mathbf{x}[n]\right)=\frac{1}{L}\sum_{l=1}^{L}\left|\alpha d(\theta_l)-\mathbf{x}^H[n]\mathbf{A}(\theta_l)\mathbf{x}[n]\right|^2, \tag{8}$$

where α is a scaling factor and $\{\theta_l\}_{l=1}^L$ are the sampled angles.

D. Problem Formulation

Based on the above problem description, in this paper we aim to design the symbol-level precoded transmit vector $\mathbf{x}[n]$ to minimize the difference between the designed and desired transmit beampatterns, while satisfying the CI-based QoS requirements of the multi-user communication system and the transmit power constraint.

It is noted that, in practical implementations, each transmit antenna uses its maximal available power to transmit the radar waveform in order to achieve the highest power efficiency [33], [34]. Thus, each element of the transmitted signal $\mathbf{x}[n]$ has a constant-modulus power constraint, i.e.,

$$|x_m[n]|=\sqrt{P_{\text{tot}}/M},\forall m=1,2,\ldots,M, \tag{9}$$

where P_{tot} is the maximum total transmit power. It should be emphasized that, for the symbol-level precoding approach, this constant-modulus power constraint holds at the symbol level (i.e., for each time slot), and thus guarantees an extraordinarily low peak-to-average power ratio (PARR), which is earnestly pursued in commercial radar systems employing low-cost and non-linear amplifiers.

For conciseness, we drop the time slot index $[n]$ in the the rest of the paper. Therefore, the optimization problem is formulated as

$$\min_{\mathbf{x},\alpha}\ \frac{1}{L}\sum_{l=1}^{L}\left|\alpha d(\theta_l)-\mathbf{x}^H\mathbf{A}(\theta_l)\mathbf{x}\right|^2 \tag{10a}$$

$$\text{s.t.}\ \ \Re\left\{\mathbf{h}_k^H\mathbf{x}e^{-j\angle s_k}\right\}\sin\Phi - \left|\Im\left\{\mathbf{h}_k^H\mathbf{x}e^{-j\angle s_k}\right\}\right|\cos\Phi\geq\beta_k,\forall k, \tag{10b}$$

$$|x_m|=\sqrt{P_{\text{tot}}/M},\forall m. \tag{10c}$$

Before the algorithm development, we first re-formulate this problem in a more compact format. It is obvious that the original problem (10) is a quadratic function in the variable α. Thus, the minimum of $f(\alpha,\mathbf{x})$ is achieved when

$$\frac{\partial f(\alpha,\mathbf{x})}{\partial\alpha}=\frac{1}{L}\sum_{l=1}^{L}\left[2\alpha d^2(\theta_l)-2d(\theta_l)\mathbf{x}^H\mathbf{A}(\theta_l)\mathbf{x}\right]=0, \tag{11}$$

which gives the optimal α as

$$\alpha^\star=\frac{\mathbf{x}^H\sum_{l=1}^{L}d(\theta_l)\mathbf{A}(\theta_l)\mathbf{x}}{\sum_{l=1}^{L}d^2(\theta_l)}. \tag{12}$$

Substituting (12) into $f(\alpha,\mathbf{x})$, the objective (10a) becomes a univariate function

$$f(\mathbf{x})=\sum_{l=1}^{L}\left|\mathbf{x}^H\mathbf{A}_l\mathbf{x}\right|^2, \tag{13}$$

where we define

$$\mathbf{A}_l\triangleq\frac{d(\theta_l)\sum_{l=1}^{L}d(\theta_l)\mathbf{A}(\theta_l)}{\sqrt{L}\sum_{l=1}^{L}d^2(\theta_l)}-\frac{\mathbf{A}(\theta_l)}{\sqrt{L}},\forall l. \tag{14}$$

In the meantime, to facilitate the following algorithm development, some basic linear algebra laws are utilized to reformulate the optimization problem in an equivalent concise form:

$$\min_{\mathbf{x}}\ \sum_{l=1}^{L}\left|\mathbf{x}^H\mathbf{A}_l\mathbf{x}\right|^2 \tag{15a}$$

$$\text{s.t.}\ \ \Re\left\{\widetilde{\mathbf{h}}_i^H\mathbf{x}\right\}\geq\gamma_i, i=1,2,\ldots,2K_{\text{u}}, \tag{15b}$$

$$|x_m|=\sqrt{P_{\text{tot}}/M},\forall m, \tag{15c}$$

where

$$\widetilde{\mathbf{h}}_{2k}^H\triangleq\mathbf{h}_k^He^{-j\angle s_k}\left(\sin\Phi+e^{-j\frac{\pi}{2}}\cos\Phi\right),\forall k, \tag{16a}$$

$$\widetilde{\mathbf{h}}_{2k-1}^H\triangleq\mathbf{h}_k^He^{-j\angle s_k}\left(\sin\Phi-e^{-j\frac{\pi}{2}}\cos\Phi\right),\forall k, \tag{16b}$$

$$\gamma_{2k}\triangleq\beta_k,\forall k,\gamma_{2k-1}\triangleq\beta_k,\forall k. \tag{16c}$$

It can be seen that the optimization problem (15) is a non-convex problem due to the quartic objective function (15a) and the constant-modulus constraint (15c), which greatly hinders finding a straightforward solution. In order to solve these difficulties, in Section III, we first utilize the PDD, MM, and BCD methods to convert the original problem into two solvable sub-problems, and then develop efficient algorithms to iteratively solve them.

III. Proposed PDD-MM-BCD Algorithm

In this section, we propose a PDD-MM-BCD algorithm to solve the non-convex problem (15). In order to tackle the constant-modulus constraint (15c), an auxiliary variable $\mathbf{v}$ is first introduced. Then, the PDD method is applied to handle the coupling constraints and variables, and the MM method is employed to tackle the complicated quartic objective function. Finally, the BCD method is utilized to iteratively solve each sub-problem. The details of the algorithm development are described as follows.

A. PDD-MM Transformation

In order to decouple the convex constraint (15b) and non-convex (15c) constraint in variable $\mathbf{x}$, the auxiliary variable $\mathbf{v}\triangleq[v_1,v_2,\ldots,v_M]^T$ is introduced to transform the optimization problem (15) to

$$\min_{\mathbf{x},\mathbf{v}}\ \sum_{l=1}^{L}\left|\mathbf{x}^H\mathbf{A}_l\mathbf{x}\right|^2 \tag{17a}$$

$$\text{s.t.}\ \ \Re\left\{\widetilde{\mathbf{h}}_i^H\mathbf{x}\right\}\geq\gamma_i,\forall i, \tag{17b}$$

$$|x_m|\leq\sqrt{P_{\text{tot}}/M},\forall m, \tag{17c}$$

$$\mathbf{x} = \mathbf{v}, \tag{17d}$$

$$|v_m| = \sqrt{P_{\text{tot}}/M}, \forall m, \tag{17e}$$

which is still a non-convex problem due to the coupling variables $\mathbf{x}$ and $\mathbf{v}$ in constraint (17d) and the constant-modulus constraint (17e) of variable $\mathbf{v}$. We then adopt the PDD method to provide a framework for iteratively solving for each variable. The PDD method is a double-loop algorithm [35], in which the inner loop utilizes the BCD approach to iteratively solve the augmented Lagrangian problem, while the outer loop updates the dual variables and/or the penalty parameters. The details are described next.

By penalizing the equality constraint (17d), the augmented Lagrangian problem of (17) is written as

$$\min_{\mathbf{x},\mathbf{v}} \quad \sum_{l=1}^{L} \left|\mathbf{x}^H \mathbf{A}_l \mathbf{x}\right|^2 + \frac{1}{2\rho} \|\mathbf{x}-\mathbf{v}\|^2 + \Re\{\boldsymbol{\mu}^H(\mathbf{x}-\mathbf{v})\} \tag{18a}$$

$$\text{s.t.} \quad \Re\left\{\widetilde{\mathbf{h}}_i^H \mathbf{x}\right\} \geq \gamma_i, \forall i, \tag{18b}$$

$$|x_m| \leq \sqrt{P_{\text{tot}}/M}, \forall m, \tag{18c}$$

$$|v_m| = \sqrt{P_{\text{tot}}/M}, \forall m, \tag{18d}$$

where $\rho > 0$ is the penalty parameter and $\boldsymbol{\mu} \in \mathbb{C}^M$ is the dual variable. In the inner loop, the BCD algorithm is utilized to iteratively solve for $\mathbf{x}$ and $\mathbf{v}$ with fixed ρ and $\boldsymbol{\mu}$. However, the complicated non-convex objective function (18a) leads to difficulties in solving each sub-problem. In order to efficiently address this issue, we use the MM method [36] and seek for a more tractable surrogate function that locally approximates and upper-bounds the objective (18a) in each iteration. The procedure for deriving the surrogate function is described below.

Using a second-order Taylor expansion as in Lemma 12 of [36], the surrogate function of a quadratic function at point $\mathbf{x}_\text{t}$ can be constructed as

$$\begin{aligned}\mathbf{x}^H \mathbf{A}_l \mathbf{x} \leq \lambda_{\mathbf{A}_l} \mathbf{x}^H \mathbf{x} + 2\Re\left\{\mathbf{x}^H(\mathbf{A}_l - \lambda_{\mathbf{A}_l}\mathbf{I}_M)\mathbf{x}_\text{t}\right\} \\ + \mathbf{x}_\text{t}^H(\lambda_{\mathbf{A}_l}\mathbf{I}_M - \mathbf{A}_l)\mathbf{x}_\text{t},\end{aligned} \tag{19}$$

where $\lambda_{\mathbf{A}_l}$ is the maximum eigenvalue of the Hermitian matrix $\mathbf{A}_l$. Thanks to the amplitude constraint (18c), the first quadratic term on the right-hand side of (19) is upper-bounded by

$$\mathbf{x}^H \mathbf{x} \leq P_{\text{tot}}. \tag{20}$$

Substituting (20) into (19), the quadratic function $\mathbf{x}^H \mathbf{A}_l \mathbf{x}$ is upper-bounded by a linear function as

$$\begin{aligned}\mathbf{x}^H \mathbf{A}_l \mathbf{x} \leq \lambda_{\mathbf{A}_l} P_{\text{tot}} + 2\Re\left\{\mathbf{x}^H(\mathbf{A}_l - \lambda_{\mathbf{A}_l}\mathbf{I}_M)\mathbf{x}_\text{t}\right\} \\ + \mathbf{x}_\text{t}^H(\lambda_{\mathbf{A}_l}\mathbf{I}_M - \mathbf{A}_l)\mathbf{x}_\text{t},\end{aligned} \tag{22}$$

which will greatly simplify the optimization and reduce the computational complexity.

Inspired by (22), we attempt to transform the first quartic term in objective function (18a) into a simple linear function by applying the second-order Taylor expansion (19) twice. The details of the derivations are presented by (21) at the bottom of this page, where we define

$$\mathbf{B} \triangleq \sum_{l=1}^{L} \text{vec}(\mathbf{A}_l)\text{vec}^H(\mathbf{A}_l), \tag{23a}$$

$$\mathbf{C} \triangleq \text{reshape}\left\{2(\mathbf{B} - \lambda_{\mathbf{B}}\mathbf{I}_{M^2})\text{vec}(\mathbf{x}_\text{t}\mathbf{x}_\text{t}^H)\right\}_{M\times M}, \tag{23b}$$

$$\mathbf{d} \triangleq 2(\mathbf{C} - \lambda_{\mathbf{C}}\mathbf{I}_M)\mathbf{x}_\text{t}, \tag{23c}$$

$$\varepsilon \triangleq \lambda_{\mathbf{C}} P_{\text{tot}} + \mathbf{x}_\text{t}^H(\lambda_{\mathbf{C}}\mathbf{I}_M - \mathbf{C})\mathbf{x}_\text{t} + \lambda_{\mathbf{B}} P_{\text{tot}}^2 \tag{23d}$$

$$+ \text{vec}^H(\mathbf{x}_\text{t}\mathbf{x}_\text{t}^H)(\lambda_{\mathbf{B}}\mathbf{I}_{M^2} - \mathbf{B})\text{vec}(\mathbf{x}_\text{t}\mathbf{x}_\text{t}^H), \tag{23e}$$

and $\lambda_{\mathbf{B}}$ and $\lambda_{\mathbf{C}}$ are the maximum eigenvalues of matrices $\mathbf{B}$ and $\mathbf{C}$, respectively. The reshape$\{\cdot\}_{M\times M}$ operation represents reshaping the vector to an $M \times M$ dimensional matrix, the vec$(\cdot)$ operation indicates vectorizing the matrix to a column vector, and vec$^H(\cdot)$ denotes the conjugate-transpose operation after vectorization. Substituting (23a) into (23b) and utilizing some basic algebra, the matrix $\mathbf{C}$ can be rewritten as $\mathbf{C} = 2\sum_{l=1}^{L} \mathbf{x}_\text{t}^H \mathbf{A}_l^H \mathbf{x}_\text{t} \mathbf{A}_l - 2\lambda_{\mathbf{B}}\mathbf{x}_\text{t}\mathbf{x}_\text{t}^H$. Since matrix $\mathbf{A}_l$ is Hermitian according to its definition in (14), it is easy to confirm that matrices $\mathbf{B}$ and $\mathbf{C}$ are also Hermitian, which enables steps (b) and (d) to utilize (19) to find the upper-bound surrogate function in (17b) and (21d). With the amplitude constraint (18c), step (c) is obtained by

$$\text{vec}^H(\mathbf{x}\mathbf{x}^H)\text{vec}(\mathbf{x}\mathbf{x}^H) \leq P_{\text{tot}}^2. \tag{24}$$

Step (d) is derived using (20). Similarly, the second quadratic term in (18a) can be upper-bounded by

$$\begin{aligned}\|\mathbf{x}-\mathbf{v}\|^2 &= \mathbf{x}^H\mathbf{x} + \mathbf{v}^H\mathbf{v} - 2\Re\left\{\mathbf{x}^H\mathbf{v}\right\} \\ &\leq P_{\text{tot}} + P_{\text{tot}} - 2\Re\left\{\mathbf{x}^H\mathbf{v}\right\}.\end{aligned} \tag{25}$$

$$\sum_{l=1}^{L} \left|\mathbf{x}^H \mathbf{A}_l \mathbf{x}\right|^2 \overset{\text{(a)}}{=} \text{vec}^H(\mathbf{x}\mathbf{x}^H)\mathbf{B}\text{vec}(\mathbf{x}\mathbf{x}^H) \tag{21a}$$

$$\overset{\text{(b)}}{\leq} \lambda_{\mathbf{B}}\text{vec}^H(\mathbf{x}\mathbf{x}^H)\text{vec}(\mathbf{x}\mathbf{x}^H) + 2\Re\left\{\text{vec}^H(\mathbf{x}\mathbf{x}^H)(\mathbf{B} - \lambda_{\mathbf{B}}\mathbf{I}_{M^2})\text{vec}(\mathbf{x}_\text{t}\mathbf{x}_\text{t}^H)\right\} + \text{vec}^H(\mathbf{x}_\text{t}\mathbf{x}_\text{t}^H)(\lambda_{\mathbf{B}}\mathbf{I}_{M^2} - \mathbf{B})\text{vec}(\mathbf{x}_\text{t}\mathbf{x}_\text{t}^H) \tag{21b}$$

$$\overset{\text{(c)}}{\leq} \lambda_{\mathbf{B}} P_{\text{tot}}^2 + \mathbf{x}^H\mathbf{C}\mathbf{x} + \text{vec}^H(\mathbf{x}_\text{t}\mathbf{x}_\text{t}^H)(\lambda_{\mathbf{B}}\mathbf{I}_{M^2} - \mathbf{B})\text{vec}(\mathbf{x}_\text{t}\mathbf{x}_\text{t}^H) \tag{21c}$$

$$\overset{\text{(d)}}{\leq} \lambda_{\mathbf{B}} P_{\text{tot}}^2 + \lambda_{\mathbf{C}}\mathbf{x}^H\mathbf{x} + 2\Re\left\{\mathbf{x}^H(\mathbf{C} - \lambda_{\mathbf{C}}\mathbf{I}_M)\mathbf{x}_\text{t}\right\} + \mathbf{x}_\text{t}^H(\lambda_{\mathbf{C}}\mathbf{I}_M - \mathbf{C})\mathbf{x}_\text{t} + \text{vec}^H(\mathbf{x}_\text{t}\mathbf{x}_\text{t}^H)(\lambda_{\mathbf{B}}\mathbf{I}_{M^2} - \mathbf{B})\text{vec}(\mathbf{x}_\text{t}\mathbf{x}_\text{t}^H) \tag{21d}$$

$$\overset{\text{(e)}}{\leq} \Re\left\{\mathbf{x}^H\mathbf{d}\right\} + \varepsilon, \tag{21e}$$

Therefore, substituting the inequalities in (21) and (25) into (18a), the upper-bound surrogate function is given by

$$\sum_{l=1}^{L}\left|\mathbf{x}^H\mathbf{A}_l\mathbf{x}\right|^2+\frac{1}{2\rho}\left\|\mathbf{x}-\mathbf{v}\right\|^2+\Re\left\{\boldsymbol{\mu}^H(\mathbf{x}-\mathbf{v})\right\}$$
$$\leq\Re\left\{\mathbf{x}^H\mathbf{d}\right\}+\varepsilon+\frac{P_{\text{tot}}}{\rho}-\frac{1}{\rho}\Re\left\{\mathbf{x}^H\mathbf{v}\right\}+\Re\left\{\boldsymbol{\mu}^H(\mathbf{x}-\mathbf{v})\right\}. \tag{26}$$

Then, ignoring the constant term $\varepsilon+P_{\text{tot}}/\rho$, the optimization problem for variables $\mathbf{x}$ and $\mathbf{v}$ in each iteration can be formulated as

$$\min_{\mathbf{x},\mathbf{v}}\ \ \Re\left\{\mathbf{x}^H\mathbf{d}-\frac{1}{\rho}\mathbf{x}^H\mathbf{v}+\boldsymbol{\mu}^H(\mathbf{x}-\mathbf{v})\right\} \tag{27a}$$
$$\text{s.t.}\ \ \Re\left\{\widetilde{\mathbf{h}}_i^H\mathbf{x}\right\}\geq\gamma_i,\forall i, \tag{27b}$$
$$|x_m|\leq\sqrt{P_{\text{tot}}/M},\forall m, \tag{27c}$$
$$|v_m|=\sqrt{P_{\text{tot}}/M},\forall m. \tag{27d}$$

A two-block BCD algorithm can be utilized to efficiently solve (27) by iteratively updating $\mathbf{x}$ and $\mathbf{v}$, as presented in the next subsection.

B. BCD Algorithm

Update $\mathbf{v}$: Ignoring the constant term $\Re\{\mathbf{x}^H(\mathbf{d}+\boldsymbol{\mu})\}$ with fixed $\mathbf{x}$, the sub-problem for updating $\mathbf{v}$ is re-arranged as

$$\max_{\mathbf{v}}\ \ \Re\left\{\left(\mathbf{x}^H+\rho\boldsymbol{\mu}^H\right)\mathbf{v}\right\} \tag{28a}$$
$$\text{s.t.}\ \ |v_m|=\sqrt{P_{\text{tot}}/M},\forall m, \tag{28b}$$

whose optimal solution can be easily obtained via a phase alignment operation, i.e.,

$$\mathbf{v}^\star=\sqrt{P_{\text{tot}}/M}e^{j\angle(\mathbf{x}+\rho\boldsymbol{\mu})}. \tag{29}$$

Update $\mathbf{x}$: With fixed $\mathbf{v}$, the sub-problem for updating $\mathbf{x}$ is given by

$$\min_{\mathbf{x}}\ \ \Re\left\{\mathbf{x}^H\widetilde{\mathbf{d}}\right\} \tag{30a}$$
$$\text{s.t.}\ \ \Re\left\{\widetilde{\mathbf{h}}_i^H\mathbf{x}\right\}\geq\gamma_i,\forall i, \tag{30b}$$
$$|x_m|\leq\sqrt{P_{\text{tot}}/M},\forall m, \tag{30c}$$

where $\widetilde{\mathbf{d}}\triangleq\mathbf{d}-\mathbf{v}/\rho+\boldsymbol{\mu}$ for brevity. Problem (31) is convex and can be solved by various standard methods such as the interior-point method [37]. However, since the double-loop iteration will lead to high computational complexity, a more efficient algorithm is developed in the remainder of this subsection, which solves the Lagrangian dual function of (31) with the aid of the Hook-Jeeves Pattern Search algorithm.

For the algorithm development, we first convert problem (31) to an equivalent real-valued form by defining

$$\overline{\mathbf{x}}\triangleq\left[\Re\{\mathbf{x}^T\},\Im\{\mathbf{x}^T\}\right]^T,\quad\overline{\mathbf{d}}\triangleq\left[\Re\{\widetilde{\mathbf{d}}^T\},\Im\{\widetilde{\mathbf{d}}^T\}\right]^T,$$
$$\overline{\mathbf{h}}_i\triangleq\left[\Re\{\widetilde{\mathbf{h}}_i^T\},\Im\{\widetilde{\mathbf{h}}_i^T\}\right]^T,\ \overline{\mathbf{e}}_m\triangleq\left[\mathbf{e}_m^T,\mathbf{0}^T\right]^T,$$
$$\boldsymbol{\Delta}_1\triangleq\begin{bmatrix}\mathbf{I}_M&\mathbf{0}\\\mathbf{0}&-\mathbf{I}_M\end{bmatrix},\qquad\boldsymbol{\Delta}_2\triangleq\begin{bmatrix}\mathbf{0}&\mathbf{I}_M\\\mathbf{I}_M&\mathbf{0}\end{bmatrix}, \tag{32}$$

where $\overline{\mathbf{e}}_m\in\mathbb{R}^{2M}$ and the auxiliary vector $\mathbf{e}_m\in\mathbb{R}^M$ is a zero-vector except the m-th entry is 1. Then, problem (31) is transformed into a real function as

$$\min_{\overline{\mathbf{x}}}\ \ \overline{\mathbf{d}}^T\boldsymbol{\Delta}_1\overline{\mathbf{x}} \tag{33a}$$
$$\text{s.t.}\ \ \overline{\mathbf{h}}_i^T\boldsymbol{\Delta}_1\overline{\mathbf{x}}\geq\gamma_i,\forall i, \tag{33b}$$
$$\left|\overline{\mathbf{e}}_m^T\boldsymbol{\Delta}_1\overline{\mathbf{x}}\right|^2+\left|\overline{\mathbf{e}}_m^T\boldsymbol{\Delta}_2\overline{\mathbf{x}}\right|^2\leq P_{\text{tot}}/M,\forall m. \tag{33c}$$

To efficiently solve problem (33), we propose to employ its Lagrangian dual function:

$$\mathcal{L}\left(\overline{\mathbf{x}},\boldsymbol{\mu},\boldsymbol{\nu}\right)=\widehat{\mathbf{d}}^T\overline{\mathbf{x}}+\boldsymbol{\mu}^T(\boldsymbol{\gamma}-\widehat{\mathbf{H}}\overline{\mathbf{x}})$$
$$+\sum_{m=1}^{M}\nu_m(\overline{\mathbf{x}}^T\mathbf{E}_m\overline{\mathbf{x}}-\frac{P_{\text{tot}}}{M}), \tag{34}$$

where

$$\widehat{\mathbf{d}}^T\triangleq\overline{\mathbf{d}}^T\boldsymbol{\Delta}_1,$$
$$\boldsymbol{\gamma}\triangleq[\gamma_1,\gamma_2,\ldots,\gamma_{2K}]^T,$$
$$\widehat{\mathbf{H}}\triangleq\left[\boldsymbol{\Delta}_1^T\overline{\mathbf{h}}_1,\ \boldsymbol{\Delta}_1^T\overline{\mathbf{h}}_2,\ \ldots,\boldsymbol{\Delta}_1^T\overline{\mathbf{h}}_{2K}\right]^T,$$
$$\mathbf{E}_m\triangleq\boldsymbol{\Delta}_1^T\overline{\mathbf{e}}_m\overline{\mathbf{e}}_m^T\boldsymbol{\Delta}_1+\boldsymbol{\Delta}_2^T\overline{\mathbf{e}}_m\overline{\mathbf{e}}_m^T\boldsymbol{\Delta}_2, \tag{35}$$

and $\boldsymbol{\mu}\in\mathbb{R}^{2K_{\text{u}}}\succeq\mathbf{0}$ and $\boldsymbol{\nu}\triangleq[\nu_1,\nu_2,\ldots,\nu_M]^T\succeq\mathbf{0}$ are the Lagrangian dual variables.

Setting $\frac{\partial\mathcal{L}}{\partial\overline{\mathbf{x}}}=\mathbf{0}$, the optimal solution $\overline{\mathbf{x}}^\star$ to problem (33) can be calculated as

$$\overline{\mathbf{x}}^\star=\frac{1}{2}\left(\sum_{m=1}^{M}\nu_m\mathbf{E}_m\right)^{-1}\left(\widehat{\mathbf{H}}^T\boldsymbol{\mu}-\widehat{\mathbf{d}}\right). \tag{36}$$

Substituting (36) into (34), the Lagrangian dual function is formulated as (36), which is presented at the bottom of this page. Since the Lagrangian dual function (36) has very simple constraints, it can be efficiently solved using standard iterative search algorithms. Given the high complexity required to calculate the first and second order partial derivatives of (28a), we adopt the derivative-free Hooke-Jeeves Pattern Search algorithm [38], which is a popular local search algorithm whose

$$\min_{\boldsymbol{\mu},\boldsymbol{\nu}}\frac{1}{4}\left(\widehat{\mathbf{H}}^T\boldsymbol{\mu}-\widehat{\mathbf{d}}\right)^T\left(\sum_{m=1}^{M}\nu_m\mathbf{E}_m\right)^{-1}\left(\widehat{\mathbf{H}}^T\boldsymbol{\mu}-\widehat{\mathbf{d}}\right)-\boldsymbol{\mu}^T\boldsymbol{\gamma}+\frac{P_{\text{tot}}}{M}\sum_{m=1}^{M}\nu_m \tag{31a}$$
$$\text{s.t.}\ \ \boldsymbol{\mu}\succeq\mathbf{0}, \tag{31b}$$
$$\boldsymbol{\nu}\succeq\mathbf{0}, \tag{31c}$$

convergence has been proven in [39]. The details are omitted due to space limitations.

After obtaining the locally optimal solution $\boldsymbol{\mu}^\star$ and $\boldsymbol{\nu}^\star$ of the Lagrangian dual problem (28), the solution $\overline{\mathbf{x}}^\star$ to the real function (33) can be obtained by (36). Then, the solution to the original problem (31) is constructed as

$$\mathbf{x}^\star = \overline{\mathbf{x}}^\star(1:M) + j\overline{\mathbf{x}}^\star(M+1:2M). \tag{37}$$

C. Summary and Analysis

Summary: Based on the above derivations, the proposed PDD-MM-BCD algorithm is straightforward and summarized in Algorithm 1, where δ_{th} is the threshold to judge the convergence, and $0 < c < 1$ is a variable for updating/decreasing the penalty parameter ρ. In the inner loop, we iteratively solve problems (28) and (30) for updating $\mathbf{x}$ and $\mathbf{v}$ until the objective value converges. In the outer loop, the penalty parameter ρ and the dual variable $\boldsymbol{\mu}$ are updated in steps 14 and 15 until the equality constraint (18d) is approximately met.

Convergence Analysis: In the inner loop for solving the augmented Lagrangian problem (18), the objective value is non-increasing since each iteration of the MM method generates non-increasing sequences [36]. In each iteration, the optimal $\mathbf{v}^\star$ is obtained in closed-form and the locally optimal $\mathbf{x}^\star$ is provided by the Hooke-Jeeves Pattern Search algorithm. Moreover, since the objective value is lower-bounded by $2\sqrt{P_{\text{tot}}/M}\|\boldsymbol{\mu}\|$, we can conclude that the solution to problem (19) in the inner loop converges. Therefore, the convergence of the PDD-based algorithm shown in Algorithm 1 can be guaranteed as analyzed in [35].

Computational Complexity Analysis: In the inner loop, the complexity for updating $\mathbf{v}^\star$ is of order $\mathcal{O}(M)$, solving problem (28) by the Hooke-Jeeves Pattern Search algorithm has complexity of order $\mathcal{O}(M^3(2K_{\text{u}}+M))$, and constructing $\mathbf{x}^\star$ is of order $\mathcal{O}(M)$. The complexity to update the penalty and dual variables is of order $\mathcal{O}(M)$. Thus, the total complexity to obtain $\mathbf{x}^\star$ is of order $\mathcal{O}(N_{\text{tot}}M^3(2K_{\text{u}}+M))$, where N_{tot} is the total number of iterations. The total computational complexity to calculate all possible $\mathbf{x}[n]$ is of order $\mathcal{O}(\Omega^{K_{\text{u}}}N_{\text{tot}}M^3(2K_{\text{u}}+M))$. As stated in [21], the complexity of the conventional block-level precoding scheme is of order $\mathcal{O}(N_{\text{tot}}K_{\text{u}}^{6.5}M^{6.5})$. We can see that for binary-PSK (BPSK) and QPSK modulations and small-scale systems, our proposed symbol-level precoding scheme is even more efficient than the block-level precoding scheme [21]. Furthermore, parallel computation can be used to simultaneously calculate the solution for each transmitted signal, which makes the proposed symbol-level precoding scheme more appealing.

Algorithm 1: Proposed PDD-MM-BCD Algorithm.

1: **Input:** $\mathbf{h}_k$, β_k, s_k, $\forall k$, $d(\theta_l)$, $\mathbf{A}(\theta_l)$, $\forall\theta_l$, L, Φ, P_{tot}, $\mathbf{E}_m, \forall m$, $\boldsymbol{\Delta}_1$, $\boldsymbol{\Delta}_2$, $0<c<1$, δ_{th}.
2: **Output:** $\mathbf{x}^\star$, $\alpha^\star$.
3: Initialize $\mathbf{x}$, $\mathbf{v}$, ρ, $\boldsymbol{\mu}$.
4: **while** $\|\mathbf{x}-\mathbf{v}\|_\infty \geq \delta_{\text{th}}$ **do**
5: Calculate the objective value f of (19a).
6: Set $\delta := 1$.
7: **while** $\delta \geq \delta_{\text{th}}$ **do**
8: $f_{\text{pre}} := f$.
9: Update $\mathbf{v}^\star$ by (30).
10: Calculate $\boldsymbol{\mu}^\star$ and $\boldsymbol{\nu}^\star$ by Hooke-Jeeves Pattern Search [38].
11: Calculate $\overline{\mathbf{x}}^\star$ by (36).
12: Construct $\mathbf{x}^\star$ by (37).
13: Calculate the objective value f of (19a).
14: $\delta := \left|\frac{f-f_{\text{pre}}}{f}\right|$.
15: **end while**
16: Update $\boldsymbol{\mu} := \boldsymbol{\mu} + (\mathbf{x}-\mathbf{v})/\rho$.
17: Update $\rho := c\rho$.
18: **end while**
19: Calculate $\alpha^\star$ by (12).
20: Return $\mathbf{x}^\star$ and $\alpha^\star$.

IV. Efficient ALM-RBFGS Algorithm

Although the proposed algorithm in the previous section is efficient for small-scale systems, its computational complexity will become unaffordable as the number of users increases due to the considerable number of iterations required by the MM-based algorithm. In order to further reduce the computational complexity for applying the proposed symbol-level precoding scheme to large-scale systems, in this section, we propose a more efficient ALM-RBFGS algorithm to solve problem (15). To benefit from existing efficient algorithms designed for unconstrained problems, we first transform this problem into the Riemannian space endowed with the constant-modulus constraint (15c), and then penalize the inequality constraints (15b) in the objective using ALM. The efficient RBFGS algorithm is further developed to solve this augmented Lagrangian problem. The details are given below.

A. Riemannian-ALM Transformation

There are two main categories of algorithms for handling the non-smooth and non-convex constant-modulus constraint (15c) on the Euclidean space. One is for non-convex relaxation-based algorithms, e.g., semi-definite relaxation (SDR) and MM. However, the SDR-based algorithm cannot be applied to problem (15) due to the coupled quartic objective function (15a) and linear constraints (15b). In addition, the MM-based algorithm as described in the previous section and other iterative non-convex relaxation-based algorithms usually require a considerable number of iterations to approximate the original objective function, which may make the computational complexity unaffordable. The other category is for algorithms based on alternating minimization, which separate each element of the variable vector from the objective function and iteratively solve for it. However, the complicated quartic objective function greatly hinders the required decomposition. Therefore, considering these difficulties in handling constraint (15c) in Euclidean space, in this subsection we use the geometric structure of the problem to solve (15) on the Riemannian space.

According to the definitions in [40], the constant-modulus constraint (15c) forms an M-dimensional complex circle manifold:

$$\mathcal{M}_{\text{cc}} = \left\{\mathbf{x}\in\mathbb{C}^M : x_m^* x_m = P_{\text{tot}}/M, \forall m\right\}, \tag{38}$$

which is a smooth Riemannian manifold equipped with an inner product defined on the tangent space:

$$T_{\mathbf{x}}\mathcal{M}_{\text{cc}} = \left\{\mathbf{z}\in\mathbb{C}^M : \Re\left\{\mathbf{z}\odot\mathbf{x}^*\right\} = \mathbf{0}_M\right\}. \tag{39}$$

Based on this definition, problem (15) is re-formulated on the Riemannian space as

$$\min_{\mathbf{x}\in\mathcal{M}_{\text{cc}}} \quad \sum_{l=1}^{L}\left|\mathbf{x}^H\mathbf{A}_l\mathbf{x}\right|^2 \tag{40a}$$

$$\text{s.t.} \quad \Re\left\{\widetilde{\mathbf{h}}_i^H\mathbf{x}\right\} \geq \gamma_i, i=1,2,\ldots,2K_{\text{u}}. \tag{40b}$$

Then, in order to convert (42) into an unconstrained problem, ALM is used to iteratively minimize the augmented Lagrangian problem and update the penalty parameter and dual variables [41]. The augmented Lagrangian function $\mathcal{L}(\mathbf{x},\rho,\boldsymbol{\mu})$ of problem (42) is given by (38) presented at the bottom of this page, where $\rho>0$ is the penalty parameter and $\boldsymbol{\mu}\triangleq[\mu_1,\mu_2,\ldots,\mu_{2K_{\text{u}}}]^T\succeq\mathbf{0}$ is the Lagrangian dual variable. The update of ρ and $\boldsymbol{\mu}$ will be discussed in Section IV-C. In the p-th iteration, the augmented Lagrangian problem with fixed penalty parameter ρ_p and dual variable $\boldsymbol{\mu}_p$ is formulated as

$$\min_{\mathbf{x}\in\mathcal{M}_{\text{cc}}} g(\mathbf{x})\triangleq\mathcal{L}(\mathbf{x},\rho_p,\boldsymbol{\mu}_p), \tag{41}$$

which is an unconstrained optimization problem on the Riemannian space $\mathcal{M}_{\text{cc}}$, and can be efficiently solved using the RBFGS algorithm described in the next subsection.

B. RBFGS Algorithm

The Riemannian manifold resembles a Euclidean space at each point, and the gradients of the cost functions, distances, angles, etc., can be measured thanks to its geometry and the Riemannian metric. Thus, well-developed algorithms for unconstrained problems in Euclidean space can be readily generalized to the Riemannian manifold. Considering the convergence speed, numerical stability, and computational complexity, we adopt the BFGS algorithm which belongs to the class of quasi-Newton methods, and refer to the BFGS algorithm generalized to the Riemannian manifold as the RBFGS algorithm [40].

To facilitate the algorithm development, we first calculate the Euclidean gradient of $g(\mathbf{x})$ as in (39) shown at the bottom of this page. Then, the Riemannian gradient grad $g(\mathbf{x})$ can be obtained by projecting the Euclidean gradient onto its corresponding tangent space as

$$\begin{aligned}\text{grad } g(\mathbf{x}) &= \text{Proj}_{\mathbf{x}}\nabla g(\mathbf{x})\\ &= \nabla g(\mathbf{x}) - \Re\left\{\nabla g(\mathbf{x})\odot\mathbf{x}^*\right\}\odot\mathbf{x}.\end{aligned} \tag{42}$$

Similar to the typical BFGS algorithm, in each iteration the RBFGS algorithm first utilizes the first-order derivative and the Hessian matrix approximation to determine the search direction, then updates the variable with a certain step size, and finally re-calculates the Hessian matrix approximation. In particular, in the q-th iteration of the RBFGS algorithm, the search direction $\boldsymbol{\eta}_q\in T_{\mathbf{x}_q}\mathcal{M}_{\text{cc}}$ is given by the Newton equation as

$$\boldsymbol{\eta}_q = -\mathbf{B}_q^{-1}\text{grad } g(\mathbf{x}_q), \tag{45}$$

where $\mathbf{B}_q$ is the approximation to the Hessian matrix obtained in the previous iteration. Then, the step size $\alpha_q\in\mathbb{R}$ is chosen by the Armijo backtracking line search method [40]. Thus, the update of $\mathbf{x}$ is given by

$$\mathbf{x}_{q+1} = \text{Retr}_{\mathbf{x}_q}\left(\alpha_q\boldsymbol{\eta}_q\right), \tag{46}$$

where $\text{Retr}_{\mathbf{x}_q}(\cdot)$ is a retraction on $\mathcal{M}_{\text{cc}}$ so that the update point remains on the manifold. According to Example 4.1.1 in [42], the low-complexity retraction on the complex circle manifold $\mathcal{M}_{\text{cc}}$ is defined as

$$\text{Retr}_{\mathbf{x}_q}\left(\alpha_q\boldsymbol{\eta}_q\right) = \sqrt{P_{\text{tot}}/M}e^{j\angle\left(\mathbf{x}_q+\alpha_q\boldsymbol{\eta}_q\right)}. \tag{47}$$

Finally, the update of the Hessian matrix approximation $\mathbf{B}$ is calculated by [40]

$$\mathbf{B}_{q+1}\boldsymbol{\xi} = \widetilde{\mathbf{B}}_q\boldsymbol{\xi} + \frac{\mathbf{y}_q^H\boldsymbol{\xi}}{\mathbf{y}_q^H\mathbf{s}_q}\mathbf{y}_q - \frac{\mathbf{s}_q^H\widetilde{\mathbf{B}}_q\boldsymbol{\xi}}{\mathbf{s}_q^H\widetilde{\mathbf{B}}_q\mathbf{s}_q}\widetilde{\mathbf{B}}_q\mathbf{s}_q, \forall\boldsymbol{\xi}\in T_{\mathbf{x}_{q+1}}\mathcal{M}_{\text{cc}}, \tag{48}$$

where we define

$$\mathbf{y}_q \triangleq \text{grad } g(\mathbf{x}_{q+1}) - \text{Trans}_{\alpha_q\boldsymbol{\eta}_q}\left(\text{grad } g(\mathbf{x}_q)\right), \tag{49a}$$

$$\mathbf{s}_q \triangleq \text{Trans}_{\alpha_q\boldsymbol{\eta}_q}\left(\alpha_q\boldsymbol{\eta}_q\right), \tag{49b}$$

$$\widetilde{\mathbf{B}}_q \triangleq \text{Trans}_{\alpha_q\boldsymbol{\eta}_q}\odot\mathbf{B}_q\odot\left(\text{Trans}_{\alpha_q\boldsymbol{\eta}_q}\right)^{-1}. \tag{49c}$$

The vector transport operation $\text{Trans}_{\alpha_q\boldsymbol{\eta}_q}(\cdot)$ is introduced since two vectors in different tangent spaces cannot be added directly on the Riemannian space. For the complex circle manifold, the vector transport is defined as

$$\begin{aligned}\text{Trans}_{\alpha_q\boldsymbol{\eta}_q}\left(\boldsymbol{\xi}_q\right) = \boldsymbol{\xi}_q - \Re\left\{\boldsymbol{\xi}_q^*\odot\left(\mathbf{x}_q+\alpha_q\boldsymbol{\eta}_q\right)\right\}\\ \odot\left(\mathbf{x}_q+\alpha_q\boldsymbol{\eta}_q\right).\end{aligned} \tag{50}$$

With the above derivations, the locally optimal solution $\mathbf{x}^\star$ to the augmented Lagrangian problem (43) can be obtained by iteratively updating (46) until convergence. This RBFGS algorithm is summarized in steps $4-13$ of Algorithm 2.

C. Parameter Update

In order to alleviate the effect of ill-conditioning and improve the robustness of this algorithm, the update for dual variables $\mu_i\geq 0,\forall i$, and penalty parameter $\rho>0$ should be carefully designed. Specifically, in the p-th iteration of the ALM-RBFGS algorithm, with the obtained solution $\mathbf{x}^\star$ to the augmented Lagrangian problem (43), the dual variable $\mu_i\geq 0,\forall i$, is updated by

$$\mu_i^{p+1} = \min\left\{\max\{0,\mu_i^p+\rho_p(\gamma_i-\Re\{\widetilde{\mathbf{h}}_i^H\mathbf{x}^\star\})\},\mu_{\max}\right\}, \tag{51}$$

$$\mathcal{L}(\mathbf{x},\rho,\boldsymbol{\mu}) = \sum_{l=1}^{L}\left|\mathbf{x}^H\mathbf{A}_l\mathbf{x}\right|^2 + \frac{\rho}{2}\sum_{i=1}^{2K_{\text{u}}}\max\left\{0,\mu_i/\rho+\gamma_i-\Re\left\{\widetilde{\mathbf{h}}_i^H\mathbf{x}\right\}\right\}^2. \tag{43}$$

$$\nabla g(\mathbf{x}) = 4\sum_{l=1}^{L}\mathbf{x}^H\mathbf{A}_l\mathbf{x}\mathbf{A}_l\mathbf{x} + \rho\sum_{i=1}^{2K_{\text{u}}}\begin{cases}\mathbf{0}, & \mu_i/\rho+\gamma_i-\Re\left\{\widetilde{\mathbf{h}}_i^H\mathbf{x}\right\}<0,\\ \left(\widetilde{\mathbf{h}}_i^H\mathbf{x}-\mu_i/\rho-\gamma_i\right)\widetilde{\mathbf{h}}_i, & \mu_i/\rho+\gamma_i-\Re\left\{\widetilde{\mathbf{h}}_i^H\mathbf{x}\right\}\geq 0.\end{cases} \tag{44}$$

where $\mu_{\max}$ is the maximum limit of μ_i to provide a good safeguard. Similarly, ρ has the maximum limit $\rho_{\max}$. Defining $\varepsilon_i = \max\{\gamma_i - \Re\{\widetilde{\mathbf{h}}_i^H \mathbf{x}^\star\}, -\frac{\mu_i}{\rho}\}$ as the violation to the i-th constraint, the maximum violation to all constraints can be expressed as $\max_i\{|\varepsilon_i|\}$. The penalty parameter ρ will be updated as

$$\rho_{p+1} = \min\{\theta_\rho \rho_p, \rho_{\max}\} \tag{52}$$

with $\theta_\rho > 1$ only when the constraint violations shrink fast enough, i.e.,

$$\max_i\{|\varepsilon_i^{p+1}|\} \geq \theta_\varepsilon \max_i\{|\varepsilon_i^p|\}, \tag{53}$$

where θ_ε represents the parameter to evaluate the shrinkage speed; otherwise ρ retains the same value as in the previous iteration. The update of the dual variables μ_i and the penalty parameter ρ is summarized as shown in steps $15-21$ of Algorithm 2.

D. Summary and Analysis

Summary: With above derivations, the procedure for the proposed ALM-RBFGS algorithm is straightforward and summarized in Algorithm 2. It is noted that the RBFGS algorithm is a local search method, thus a warm-start is preferable. Intuitively, the solution to the scenario that does not consider communication services is a great choice. The optimization problem for initialization is thus expressed as

$$\min_{\mathbf{x}\in\mathcal{M}_{\text{cc}}} \sum_{l=1}^{L} \left|\mathbf{x}^H \mathbf{A}_l \mathbf{x}\right|^2, \tag{54}$$

which can be efficiently solved by the RBFGS algorithm as in steps $4-12$ with a random feasible initial point $\mathbf{x}_0 \in \mathcal{M}_{\text{cc}}$. Given an initial point by solving problem (54), the solution $\mathbf{x}^\star$ to the augmented Lagrangian problem (43), the penalty parameter ρ, and the dual variable $\boldsymbol{\mu}$ are iteratively updated until convergence is achieved.

Computational Complexity Analysis: The computational complexity of using the RBFGS algorithm to update $\mathbf{x}$ is of order $\mathcal{O}\{M^3\}$, and the computational complexity of updating $\boldsymbol{\mu}$ and ρ is of order $\mathcal{O}\{4K_{\text{u}}M\}$. Therefore, the total computational complexity of the proposed ALM-RBFGS algorithm is of order $\mathcal{O}\{\Omega^{K_{\text{u}}} N_{\text{tot}}(M^3 + 4K_{\text{u}}M)\}$. It can be seen that the ALM-RBFGS algorithm is theoretically more efficient than the PDD-MM-BCD algorithm. Moreover, the numerical results in the next section will show that the ALM-RBFGS algorithm requires much fewer iterations and less execution time, which makes it a more practical implementation for large-scale systems.

Algorithm 2: Efficient ALM-RBFGS Algorithm.

1: **Input:** $\mathbf{h}_k$, β_k, s_k, $\forall k$, $d(\theta_l)$, $\mathbf{A}(\theta_l)$, $\forall \theta_l$, L, Φ, P_{tot}, $\delta_{\text{th}}, \theta_\rho > 1$, $0 < \theta_\varepsilon < 1$, $\rho_{\max}$, $\mu_{\max}$.
2: **Output:** $\mathbf{x}^\star$, $\alpha^\star$.
3: Initialize $\mathbf{x}_0 \in \mathcal{M}_{\text{cc}}$, $\mathbf{B}_0 := \mathbf{I}_M$, ρ_0, μ_i^0, $p := 0$, $\delta_{\text{out}} > \delta_{\text{th}}$.
4: Obtain the initial point $\mathbf{x}_0^{\text{out}}$ and $\mathbf{x}_0^{\text{in}}$ by solving (54).
5: **while** $\delta_{\text{out}} > \delta_{\text{th}}$ **do**
6: Initialize $q := 0$, grad $g(\mathbf{x}_0)$, $\delta_{\text{in}} > \delta_{\text{th}}$.
7: **while** $\delta_{\text{in}} > \delta_{\text{th}}$ **do**
8: Obtain $\boldsymbol{\eta}_q \in \mathcal{M}_{\text{cc}}$ by (45).
9: Calculate the stepsize α_q by Armijo backtracking line search method [40].
10: Update $\mathbf{x}_{q+1}^{\text{in}}$ by (46).
11: Calculate the Riemannian gradient grad $g(\mathbf{x}_{q+1}^{\text{in}})$ by (44).
12: Update the Hessian approximation $\mathbf{B}_{q+1}$ by (48).
13: $\delta_{\text{in}} := \|\mathbf{x}_{q+1}^{\text{in}} - \mathbf{x}_q^{\text{in}}\|$.
14: $q := q + 1$.
15: **end while**
16: $\mathbf{x}_{p+1}^{\text{out}} := \mathbf{x}_q^{\text{in}}$.
17: $\mu_i^{p+1} := \min\{\max\{0, \mu_i^p + \rho_p(\gamma_i - \Re\{\widetilde{\mathbf{h}}_i^H \mathbf{x}_{p+1}^{\text{out}}\})\}, \mu_{\max}\}$.
18: $\varepsilon_i^{p+1} := \max\{\gamma_i - \Re\{\widetilde{\mathbf{h}}_i^H \mathbf{x}_{p+1}^{\text{out}}\}, -\frac{\mu_i^p}{\rho_p}\}$.
19: **if** $p = 0$ or $\max\{|\varepsilon_i^{p+1}|, \forall i\} \leq \theta_\varepsilon \max\{|\varepsilon_i^p|, \forall i\}$ **then**
20: $\rho_{p+1} := \rho_p$.
21: **else**
22: $\rho_{p+1} := \min\{\theta_\rho \rho_p, \rho_{\max}\}$.
23: **end if**
24: $\delta_{\text{out}} := \|\mathbf{x}_{p+1}^{\text{out}} - \mathbf{x}_p^{\text{out}}\|$.
25: $p := p + 1$.
26: **end while**
27: $\mathbf{x}^\star := \mathbf{x}_p^{\text{out}}$.
28: Calculate $\alpha^\star$ by (12).
29: Return $\mathbf{x}^\star$ and $\alpha^\star$.

V. Extensions for Doppler Processing

As mentioned previously, the approach presented in this paper focuses only on the spatial properties of the radar, and assumes the Doppler component is negligible. When the targets of interest are rapidly moving, Doppler effects must be taken into account, and the temporal characteristics of the radar waveform come into play. Given the symbol-level nature of the communication constraints, this requires non-trivial extensions to the approaches proposed herein. In this section, we briefly discuss two possible approaches that could be taken to tackle this problem.

Standard radar implementations employ temporal pulse sequences whose correlation properties are carefully chosen to trade-off resolution in range and Doppler. In MIMO radar, these become sequences of vector pulses with further considerations of spatial correlation, which leads to designs that also must take into account the spatial response (e.g., such as the beampattern as considered here). Since symbol-level precoding is by definition focused on transmission of a single symbol, modifications are necessary when designing symbol sequences.

One approach would be to use the idea of *waveform similarity*, which quantifies the difference between the transmitted waveform and some ideal reference waveforms with desirable space-time correlation properties. In particular, let $\widetilde{\mathbf{x}}_0 \triangleq [\widetilde{\mathbf{x}}_0^T[1], \ldots, \widetilde{\mathbf{x}}_0^T[N]]^T \in \mathbb{C}^{NM}$ represent the reference waveform, where N denotes the number of radar pulses. The waveform optimization problem could then be formulated as

$$\min_{\mathbf{x}[1],\ldots,\mathbf{x}[N]} \quad \sum_{n=1}^{N} \left\|\mathbf{x}[n] - \widetilde{\mathbf{x}}_0[n]\right\|^2 \tag{55a}$$

$$\text{s.t.} \quad \Re\left\{\widetilde{\mathbf{h}}_i^H \mathbf{x}[n]\right\} \geq \gamma_i, \forall i, n, \tag{55b}$$

$$|x_m[n]| = \sqrt{P_{\text{tot}}/M}, \forall m, n. \tag{55c}$$

This problem can be equivalently divided into N sub-problems, each of which has a form similar to the one given in problem (15), and thus could be solved using the proposed algorithms with some straightforward modifications.

Instead of using a reference waveform, a second approach would be to again pose the problem as one of precoding the entire space-time waveform as in (55), but with an objective function and constraints that address the dual radar-communications functionality. As an example, for the communications centric approach considered in this paper, the radar objective could involve matching a desired angle-Doppler spectrum or ambiguity function on the radar side, and the communication constraints could be imposed on the symbols over the entire block. In this case, the "symbol"-level precoding would involve a super-symbol that is decoded as a block rather than individually (for a discussion of implementing symbol-level precoding over a block of data, see [32]). This would further allow the corresponding constructive regions to account for built-in temporal redundancy due to channel coding as well, since certain codewords would not be valid.

The details of extensions such as those discussed above are beyond the scope of this paper, but they serve to emphasize the generality of the symbol-level precoding idea to DFRC systems.

VI. Simulation Results

In this section, we provide extensive simulation results to evaluate the performance of the proposed symbol-level precoding designs for DFRC systems. To demonstrate the advantages of our proposed symbol-level precoding algorithms, the state-of-the-art block-level precoding approaches for DFRC systems in [16] and [21] are included for comparison. The instantaneous transmit beampatterns are first plotted in Section VI-A to intuitively illustrate the advantages of the proposed schemes in radar sensing. Then, the radar sensing and multi-user communication performance is quantitatively evaluated in Section VI-B to demonstrate the superiority of the proposed symbol-level precoding schemes. Finally, the comparisons of convergence and computational complexity are shown in Section VI-C to illustrate the efficiency of the proposed algorithms. The simulations are carried out using Matlab 2020b on a PC with an Intel Core i7-9700 CPU and 32 GB of RAM.

In the simulations, we assume that the noise power and QoS requirements for each communication user are the same, i.e., $\sigma^2 = \sigma_k^2 = 10\text{dBm}, \beta = \beta_k, \forall k$. For a fair comparison with the conventional block-level precoding schemes, in which the SINR threshold is Γ, we set the QoS requirement of our proposed schemes as $\beta = \sigma \sin\Phi\sqrt{\Gamma}$. The following simulation will show that this setting makes the communication constraint (3) stricter than the block-level precoding counterpart. The noise power in the received radar signal is $\sigma_z^2 = 20\text{dBm}$, and the total transmit power is set as $P_{\text{tot}} = 30\text{dBm}$. The BS is equipped with $M = 10$ antennas with antenna spacing $\Delta = \lambda/2$. QPSK constellation symbols are assumed for all users. We assume $K_{\text{t}} = 3$ targets at the locations $\theta_1 = -40^\circ$, $\theta_2 = 0^\circ$, and $\theta_3 = 40^\circ$, respectively, with the same amplitudes $\beta_\theta = 1$. The ideal beampattern is thus given by

$$d(\theta) = \begin{cases} 1, & \theta_i - \frac{\Delta_\theta}{2} \leq \theta \leq \theta_i + \frac{\Delta_\theta}{2}, i = 1, 2, 3, \\ 0, & \text{otherwise}, \end{cases} \tag{56}$$

where $\Delta_\theta = 10^\circ$ is the beam width in the desired directions. The direction grids $\{\theta_l\}_{l=1}^L$ are uniformly sampled from -90° to 90° with a resolution of 1°. The scaling parameters are set as $c = 0.8$, $\theta_\rho = 1.1$, and $\theta_\epsilon = 0.6$. In addition, the convergence threshold δ_{th} is set as 10^{-5} in the simulations.

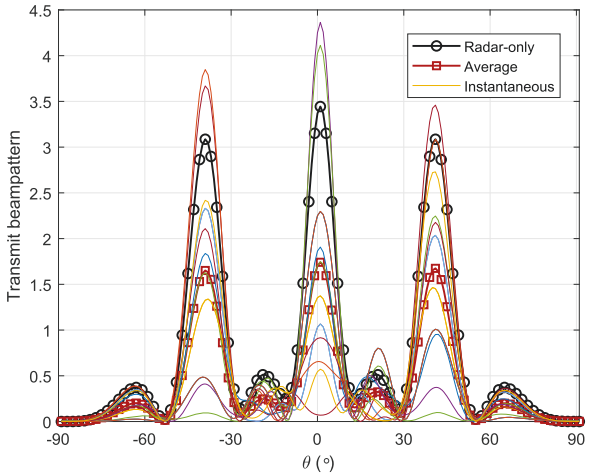

(a) Conventional block-level precoding scheme [21].

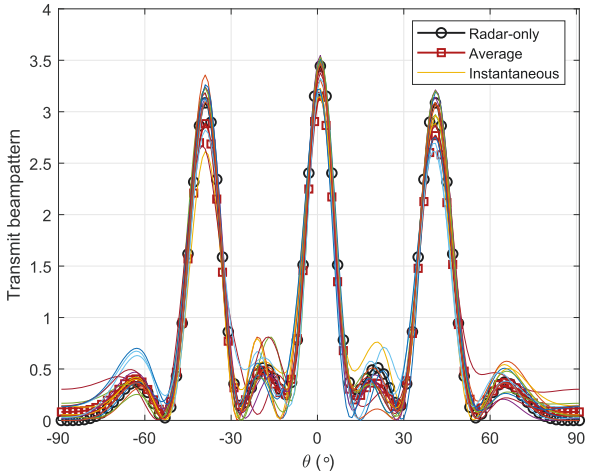

(b) Proposed symbol-level precoding scheme (PDD-MM-BCD).

Fig. 3. Instantaneous transmit beampatterns (Black lines represent the radar-only benchmark [33], other colored lines represent the obtained beampatterns in different time slots except for the red lines with square markers denoting their average).

A. Instantaneous Transmit Beampattern

The instantaneous transmit beampatterns are shown in Fig. 3 for the block-level precoding scheme in [21] and the proposed symbol-level precoding approach using the PDD-MM-BCD algorithm, where black lines with circle markers represent the radar-only benchmark [33], and other colored lines denote the obtained transmit beampatterns in different time slots, except for

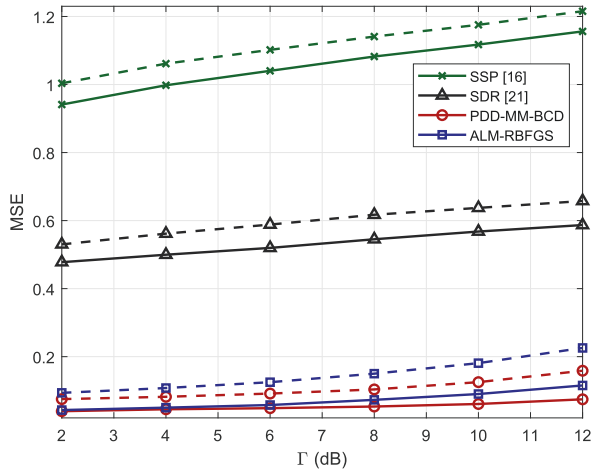

Fig. 4. Transmit beampattern MSE versus the QoS requirements of multi-user communication Γ (Solid lines represent the $K_{\rm u}=3$ scenario, and dashed lines represent the $K_{\rm u}=4$ scenario).

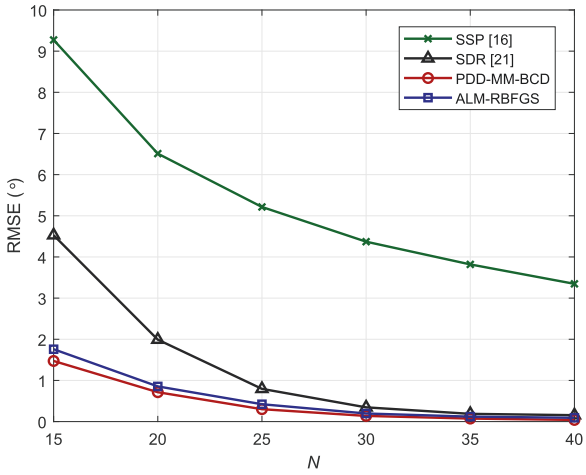

Fig. 5. Angle estimation RMSE versus the number of collected signals N ($K_{\rm u}=3$ and $\Gamma=6$dB).

the red lines with square markers which denote their average. The QoS requirement for the $K_{\rm u}=3$ communication users is set as $\Gamma=6$dB. It is clear that the instantaneous transmit beampatterns of the proposed symbol-level precoding scheme in Fig. 3(b) always maintain satisfactory similarity with the ideal beampattern in all time slots; i.e., they are all clustered around the radar-only benchmark, while the block-level precoding counterparts have dramatic fluctuations as shown in Fig. 3(a). Furthermore, we can observe that the average transmit beampattern of these snapshots in Fig. 3(b) for symbol-level precoding is also better than that in Fig. 3(a) for block-level precoding. Thus, we can conclude that the symbol-level precoding technique provides significantly better consistency in generating well-formed beampatterns for each time slot and can achieve better average transmit beampatterns with limited samples. In addition to the qualitative results in Fig. 3, quantitative evaluations of the target detection and parameter estimation performance will be shown in the next subsection to verify the advantages of the proposed symbol-level precoding scheme.

B. Comparisons of Radar and Communication Performance

In this subsection, we first evaluate the radar performance in terms of transmit beampattern MSE in Fig. 4. The transmit beampattern MSE is defined as the average squared error between the optimal radar-only transmit beampattern [33] and the obtained instantaneous transmit beampattern:

$$\text{MSE}=\mathbb{E}\left\{\frac{1}{L}\sum_{l=1}^{L}\left|\mathbf{a}^H(\theta_l)\mathbf{R}^{\star}\mathbf{a}(\theta_l)-\mathbf{x}^H[n]\mathbf{A}(\theta_l)\mathbf{x}[n]\right|^2\right\}, \tag{57}$$

where $\mathbf{R}^{\star}$ is the optimal covariance matrix for the radar-only scenario. In Fig. 4, the MSE versus the communication QoS requirements Γ is plotted for $K_{\rm u}=3$ (solid lines) and $K_{\rm u}=4$ (dashed lines) scenarios, where "SSP [16]" and "SDR [21]" respectively denote the block-level precoding schemes solved by the sum-square penalty based algorithm [16] and the SDR-based algorithm [21], "PDD-MM-BCD" and "ALM-RBFGS" denote the proposed symbol-level precoding designs solved by Algorithm 1 and Algorithm 2, respectively. Not surprisingly, the MSE for all schemes increases with larger Γ and $K_{\rm u}$, which shows the performance trade-off between radar sensing and multi-user communications. In addition, the proposed symbol-level precoding algorithms can dramatically reduce the transmit beampattern MSE compared with the conventional block-level precoding schemes, which results primarily for the following two reasons: *i)* The proposed symbol-level precoding approaches focus on the instantaneous transmit beampatterns by designing the transmitted signal in each time slot, while the block-level precoding methods [16], [21] only consider the average transmit beampattern by optimizing the second-order statistics of the transmitted signals. *ii)* Our developed non-linear symbol-level precoding designs can exploit more DoFs than the linear block-level precoding approach. We also observe that the performance of SDR [21] is better than that of SSP [16], since the former scheme transmits both the precoded communication symbols and the radar waveform, which can exploit more DoFs for radar sensing than the latter scheme. Furthermore, compared with the PDD-MM-BCD algorithm, only a slight performance loss is observed for the ALM-RBFGS algorithm, and the loss grows as Γ increases since stronger penalty terms to guarantee higher communication QoS requirements affect the optimization of the radar performance objective.

Next, in order to illustrate the advantages of the proposed symbol-level precoding designs in guaranteeing preferable target angular estimation performance with limited radar samples, we show the target angular estimation performance versus the number of collected samples in Fig. 5. The popular generalized likelihood ratio test (GLRT) [43] is used to process the collected signals and estimate the angles $\{\widehat{\theta}_{k_{\rm t}}\}_1^{K_{\rm t}}$. Before providing a brief review of the GLRT method, we first define $\mathbf{X}\triangleq[\mathbf{x}[1],\ldots,\mathbf{x}[N]]$, $\mathbf{Y}\triangleq[\mathbf{y}[1],\ldots,\mathbf{y}[N]]$, $\mathbf{Z}\triangleq[\mathbf{z}[1],\ldots,\mathbf{z}[N]]$, where N is the number of collected samples, and $\mathbf{r}^H(\theta)\triangleq\mathbf{a}^H(\theta)\mathbf{X}$. The typical GLRT method is developed to test if there exists a target at the angular location θ, thus the following hypothesis testing problem is considered

$$\begin{cases} H_0:\mathbf{Y}=\mathbf{Z}, \\ H_1:\mathbf{Y}=\beta_\theta\mathbf{a}(\theta)\mathbf{r}^H(\theta)+\mathbf{Z}. \end{cases} \tag{58}$$

The generalized-likelihood ratio (GLR) at the angular direction θ is defined by

$$\rho_{\mathrm{G}}(\theta) = 1 - \left[\frac{\max f(\mathbf{Y}|H_0)}{\max f(\mathbf{Y}|H_1)}\right]^{1/N}, \tag{59}$$

where $f(\mathbf{Y}|H_i)$ is the probability density function (PDF) of $\mathbf{Y}$ under the hypothesis $H_i, i = 0, 1$. According to (59), the GLR at each $\theta \in [-90^\circ, 90^\circ]$ with a certain resolution can be calculated. Then, the angular direction of a target can be estimated by

$$\widehat{\theta}_1 = \arg\max_{\theta} \rho_{\mathrm{G}}(\theta). \tag{60}$$

For the case with multiple targets, the iterative GLRT (iGLRT) [43] is used to estimate the angular directions of the K_{t} targets as follows. Suppose we have detected and located κ targets at the angles $\{\theta_{k_{\mathrm{t}}}\}_1^{\kappa}$, and we are testing if there is a $(\kappa+1)$-th target. The corresponding hypothesis testing problem is

$$\begin{cases} H_{\kappa} : \mathbf{Y} = \sum_{k_{\mathrm{t}}=1}^{\kappa} \beta_{k_{\mathrm{t}}} \mathbf{a}(\theta_{k_{\mathrm{t}}}) \mathbf{r}^H(\theta_{k_{\mathrm{t}}}) + \mathbf{Z}, \\ H_{\kappa+1} : \mathbf{Y} = \beta_{\theta} \mathbf{a}(\theta) \mathbf{r}(\theta) + \sum_{k_{\mathrm{t}}=1}^{\kappa} \beta_{k_{\mathrm{t}}} \mathbf{a}(\theta_{k_{\mathrm{t}}}) \mathbf{r}^H(\theta_{k_{\mathrm{t}}}) + \mathbf{Z}, \end{cases} \tag{61}$$

and the corresponding conditional GLR (cGLR) [43] is defined by

$$\rho_{\mathrm{G}}(\theta|\{\widehat{\theta}_{k_{\mathrm{t}}}\}_1^{\kappa}) = 1 - \left[\frac{\max f(\mathbf{Y}|H_{\kappa})}{\max f(\mathbf{Y}|H_{\kappa+1})}\right]^{1/N}. \tag{62}$$

With the cGLR in (62), the angle of the $(\kappa+1)$-th target is estimated by

$$\widehat{\theta}_{\kappa+1} = \arg\max_{\theta} \rho_{\mathrm{G}}(\theta|\{\widehat{\theta}_{k_{\mathrm{t}}}\}_1^{\kappa}). \tag{63}$$

Detailed derivations and expressions for $\rho_{\mathrm{G}}(\theta)$ in (59) and $\rho_{\mathrm{G}}(\theta|\{\widehat{\theta}_{k_{\mathrm{t}}}\}_1^{\kappa})$ in (62) can be found in [43] and are omitted here for brevity. In summary, we first use (60) to detect the first target and estimate its angle. Then, the remaining $K_{\mathrm{t}} - 1$ targets are conditionally detected and estimated by (63) in sequence.

The target angular estimation performance is evaluated in terms of the root-mean-square-error (RMSE) of the estimated target angles, which is defined as

$$\mathrm{RMSE} = \sqrt{\mathbb{E}\left\{\frac{1}{K_{\mathrm{t}}} \sum_{k_{\mathrm{t}}=1}^{K_{\mathrm{t}}} \left(\theta_{k_{\mathrm{t}}} - \widehat{\theta}_{k_{\mathrm{t}}}\right)^2\right\}}, \tag{64}$$

where $\theta_{k_{\mathrm{t}}}$ is the actual angle and $\widehat{\theta}_{k_{\mathrm{t}}}$ is the estimated angle of the k_{t}-th target. From Fig. 5, we see that as the number of collected samples increases, the estimation accuracy improves for all schemes. However, our proposed algorithms always provide better angular estimation performance than [16] and [21] since the non-linear symbol-level precoding designs can exploit more DoFs than the linear block-level precoding counterparts, despite the fact that they also impose stricter communication constraints. It is also worth noting that with very few collected samples, e.g., $N = 15$, the proposed schemes can provide much lower RMSE, which reveals the potentials of the symbol-level precoding designs in fast radar sensing cases.

In order to evaluate the target detection performance, we present the receiver operating characteristic (ROC) by plotting the detection probability P_{D} versus the false alarm probability P_{FA} in Fig. 6. In particular, the $(\kappa+1)$-th target is detected by testing

$$\rho_{\mathrm{G}}(\theta|\{\widehat{\theta}_{k_{\mathrm{t}}}\}_1^{\kappa}) \underset{H_{\kappa}}{\overset{H_{\kappa+1}}{\gtrless}} \delta, \tag{65}$$

where δ is the threshold which determines P_{FA} and P_{D}. In addition, it can be observed that with the same false alarm probability, e.g., 10^{-5}, both the proposed PDD-MM-BCD and ALM-RBFGS algorithms achieve much higher detection probability than the two block-level approaches, which illustrates the superiority of the proposed symbol-level precoding scheme for target detection.

Finally, we evaluate the communication performance in terms of SER in Fig. 7, where the same settings as in Fig. 4 are assumed. Since the communication constraints of the symbol-level precoding algorithms are stricter than those of the block-level precoding methods, a lower SER for the symbol-level approaches is observed in Fig. 7. Moreover, since the constraints of the communication QoS are incorporated into the objective function as a penalty term in [16], they cannot always be satisfied in

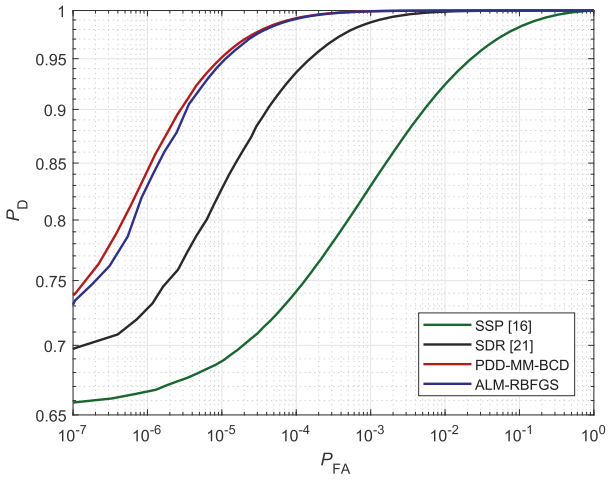

Fig. 6. Detection probability versus false alarm probability ($K_{\mathrm{u}} = 3$, $\Gamma = 6$ dB, and $N = 15$).

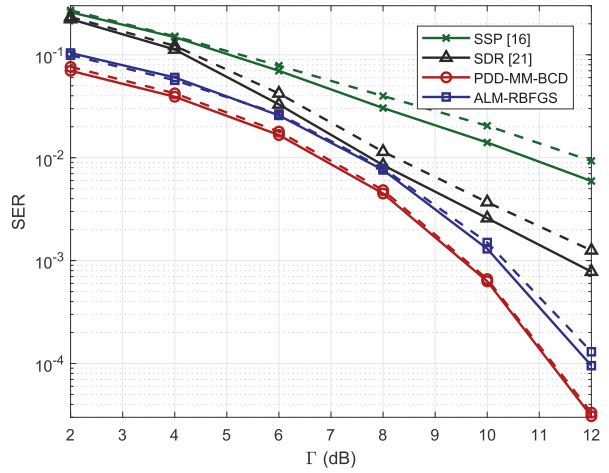

Fig. 7. Average SER versus the QoS requirements of multi-user communication Γ (Solid lines represent the $K_{\mathrm{u}} = 3$ scenario, and dashed lines represent the $K_{\mathrm{u}} = 4$ scenario).

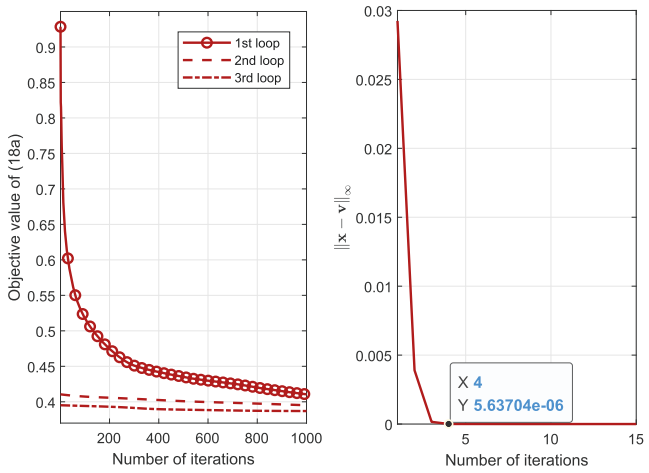

(a) Inner loop. (b) Outer loop.

Fig. 8. Convergence of PDD-MM-BCD algorithm.

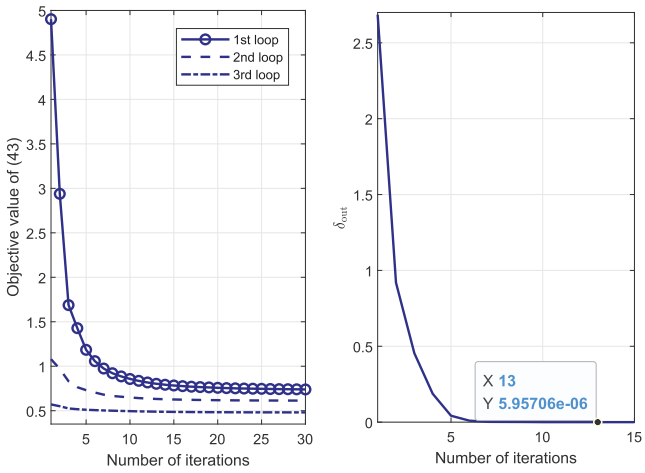

(a) Inner loop. (b) Outer loop.

Fig. 9. Convergence of ALM-RBFGS algorithm.

the optimizations, which causes worse communication performance, i.e., higher SER. In addition, we see that the SER performance of the ALM-RBFGS algorithm is worse than that for the PDD-MM-BCD algorithm since violations of the communication constraints exist in optimizing the augmented Lagrangian problem (43). However, the slight performance loss is acceptable especially considering the significant computational complexity reduction as illustrated in the next subsection. Furthermore, the ALM-RBFGS algorithm still provides better SER performance than the block-level precoding approaches, which makes it a very competitive candidate for DFRC systems.

C. Comparisons of Convergence and Complexity

The convergence performance of the proposed PDD-MM-BCD algorithm is illustrated in Fig. 8, where the QoS requirement for the $K_{\text{u}} = 3$ communication users is set as $\Gamma = 6$dB. Fig. 8(a) shows the convergence of the objective value (18a) in the inner loop, where the curve with circle markers denotes the initial loop. It can be seen that the inner loop monotonically converges within a limited number of iterations, and the required number of iterations sharply decreases after the initial loop. The convergence of the outer loop is presented in Fig. 8(b), where we see that the error of the equality constraint (17d) quickly converges within 4 iterations. Furthermore, with the aid of the more efficient Hooke-Jeeves Pattern Search algorithm rather than the CVX toolbox, the computational complexity of the entire PDD-MM-BCD algorithm is manageable for moderate-scale systems.

The convergence performance of the proposed ALM-RBFGS algorithm is shown in Fig. 9, where the settings are the same as in Fig. 8. In particular, Fig. 9(a) plots the convergence of the objective value (43) obtained by the RBFGS algorithm, and Fig. 9(b) presents the convergence of ALM in the outer loop, where δ_{out} is the difference of two consecutive iterations as defined in step 22 of Algorithm 2. The convergence of both the inner and outer loops is very rapid. Moreover, comparing Fig. 9(a) with Fig. 8(a), we can easily conclude that the ALM-RBFGS algorithm requires orders of magnitude fewer iterations in solving the augmented Lagrangian problem. This is because the ALM-RBFGS algorithm directly solves the quartic objective function rather than iteratively approximating it as in the PDD-MM-BCD algorithm. Thus, the total computational complexity of the ALM-RBFGS algorithm will be much lower than the PDD-MM-BCD algorithm.

TABLE I
AVERAGE EXECUTION TIME (SECONDS) TO OBTAIN THE PRECODED TRANSMIT VECTOR

K_{u}	2	3	4	5	6
PDD-MM-BCD	5.57	7.52	8.37	8.47	9.91
ALM-RBFGS	0.149	0.158	0.189	0.203	0.233

Finally, to provide a more intuitive and direct comparison of complexity, the average execution time required to obtain the precoded transmit vector using the PDD-MM-BCD and ALM-RBFGS algorithms is presented in Table I. We see that the execution time increases as the number of users increases, since the increasing number of constraints results in a larger number of variables and more iterations. Comparing the two proposed algorithms, it can be seen that the ALM-RBFGS approach is much more efficient and only requires about 2% of the execution time of the PDD-MM-BCD method, which makes the performance loss shown in the previous subsections acceptable.

VII. CONCLUSIONS

In this paper, we introduced the novel symbol-level precoding technique to DFRC systems and investigated the associated waveform designs. The squared error between the designed and desired beampatterns was minimized while satisfying symbol-level constraints on the communication QoS and constant-modulus power. We proposed two efficient algorithms to solve this non-convex problem with different trade-offs in terms of performance and complexity. Simulation results shown that the proposed symbol-level precoding approach provides more accurate angle estimation and better target detection performance with limited collected signals, as well as lower SER for multi-user communications compared with conventional block-level precoding methods. These results reveal the immense potential of symbol-level precoding in DFRC systems. Motivated by this

initial work, more complicated symbol-level precoding based DFRC systems deserve further investigation, e.g., in hostile radar sensing environments with the presence of clutter or jamming signals. In addition to the considered beampattern squared error metric, the work can be extended to use other radar waveform design metrics such as mutual information, SINR, the Cramér-Rao bound, etc., to explore the performance improvements in radar sensing offered by symbol-level precoding. Extensions to the case with non-negligible Doppler as discussed in Section V also warrant further attention.

REFERENCES

[1] L. Zheng, M. Lops, Y. C. Eldar, and X. Wang, "Radar and communication coexistence: An overview: A review of recent methods," *IEEE Signal Process. Mag.*, vol. 36, no. 5, pp. 85–99, Sep. 2019.

[2] D. Ma, N. Shlezinger, T. Huang, Y. Liu, and Y. C. Eldar, "Joint radar-communications strategies for autonomous vehicles: Combining two key automotive technologies," *IEEE Signal Process. Mag.*, vol. 37, no. 4, pp. 85–97, Jul. 2020.

[3] F. Liu, C. Masouros, A. P. Petropulu, H. Griffiths, and L. Hanzo, "Joint radar and communication design: Applications, state-of-the-art, and the road ahead," *IEEE Trans. Commun.*, vol. 68, no. 6, pp. 3834–3862, Jun. 2020.

[4] L. Zheng, M. Lops, and X. Wang, "Adaptive interference removal for uncoordinated radar/communication coexistence," *IEEE J. Sel. Topics Signal Process.*, vol. 12, no. 1, pp. 45–60, Feb. 2018.

[5] F. Liu, C. Masouros, A. Li, T. Ratnarajah, and J. Zhou, "MIMO radar and cellular coexistence: A power-efficient approach enabled by interference exploitation," *IEEE Trans. Signal Process.*, vol. 66, no. 14, pp. 3681–3695, Jul. 2018.

[6] J. A. Zhang, M. L. Rahman, X. Huang, S. Chen, Y. J. Guo, and R. W. Heath, "Perceptive mobile networks: Cellular networks with radio vision via joint communication and radar sensing," *IEEE Veh. Technol. Mag.*, vol. 16, no. 2, pp. 20–30, Jun. 2021.

[7] J. Li and P. Stoica, "MIMO radar with colocated antennas," *IEEE Signal Process. Mag.*, vol. 24, no. 5, pp. 106–114, Sep. 2007.

[8] K. Wu, J. A. Zhang, X. Huang, Y. J. Guo, and R. W. Heath, "Waveform design and accurate channel estimation for frequency-hopping MIMO radar-based communications," *IEEE Trans. Commun.*, vol. 69, no. 2, pp. 1244–1258, Feb. 2021.

[9] A. Hassanien, M. G. Amin, Y. D. Zhang, and F. Ahmad, "Dual-function radar-communications: Information embedding using sidelobe control and waveform diversity," *IEEE Trans. Signal Process.*, vol. 64, no. 8, pp. 2168–2181, Apr. 2016.

[10] P. M. McCormick, S. D. Blunt, and J. G. Metcalf, "Simultaneous radar and communications emissions from a common aperture, Part I: Theory," in *Proc. IEEE Radar Conf.*, Seattle, USA, 2017, pp. 1685–1690.

[11] J. Qian, M. Lops, L. Zhang, X. Wang, and Z. He, "Joint system design for coexistence of MIMO radar and MIMO communication," *IEEE Trans. Signal Process.*, vol. 66, no. 13, pp. 3504–3519, Jul. 2018.

[12] B. Tang, H. Wang, L. Qin, and L. Li, "Waveform design for dual-function MIMO radar-communication systems," in *Proc. IEEE Sensor Array Multichannel Signal Process. Workshop*, Hangzhou, China, 2020, pp. 1–5.

[13] P. Kumari, S. A. Vorobyov, and R. W. Heath, "Adaptive virtual waveform design for millimeter-wave joint communication-radar," *IEEE Trans. Signal Process.*, vol. 68, pp. 715–730, Nov. 2019, doi: 10.1109/TSP.2019.2956689.

[14] F. Liu, C. Masouros, T. Ratnarajah, and A. Petropulu, "On range sidelobe reduction for dual-functional radar-communication waveforms," *IEEE Wireless Commun. Lett.*, vol. 9, no. 9, pp. 1572–1576, Sep. 2020.

[15] F. Liu, L. Zhou, C. Masouros, A. Li, W. Luo, and A. Petropulu, "Toward dual-functional radar-communication systems: Optimal waveform design," *IEEE Trans. Signal Process.*, vol. 66, no. 16, pp. 4264–4279, Aug. 2018.

[16] F. Liu, C. Masouros, A. Li, H. Sun, and L. Hanzo, "MU-MIMO communications with MIMO radar: From co-existence to joint transmission," *IEEE Trans. Wireless Commun.*, vol. 17, no. 4, pp. 2755–2770, Apr. 2018.

[17] Z. Cheng, B. Liao, and Z. He, "Hybrid transceiver design for dual-functional radar-communication system," in *Proc. IEEE Sensor Array Multichannel Signal Process. Workshop*, Hangzhou, China, 2020, pp. 1–5.

[18] W. Yuan, F. Liu, C. Masouros, J. Yuan, D. W. K. Ng, and N. G. Prelcic, "Bayesian predictive beamforming for vehicular networks: A low-overhead joint radar-communication approach," *IEEE Trans. Wireless Commun.*, vol. 20, no. 3, pp. 1442–1456, Mar. 2021.

[19] C. Xu, B. Clerckx, and J. Zhang, "Multi-antenna joint radar and communications: Precoder optimization and weighted sum-rate vs probing power tradeoff," *IEEE Access*, vol. 8, pp. 173974–173982, Sep. 2020, doi: 10.1109/ACCESS.2020.3025156.

[20] N. Su, F. Liu, and C. Masouros, "Secure radar-communication systems with malicious targets: Integrating radar, communications and jamming functionalities," *IEEE Trans. Wireless Commun.*, vol. 20, no. 1, pp. 83–95, Jan. 2021.

[21] X. Liu, T. Huang, N. Shlezinger, Y. Liu, J. Zhou, and Y. C. Eldar, "Joint transmit beamforming for multiuser MIMO communications and MIMO radar," *IEEE Trans. Signal Process.*, vol. 68, pp. 3929–3944, Jun. 2020, doi: 10.1109/TSP.2020.3004739.

[22] L. Chen, F. Liu, J. Liu, and C. Masouros, "Composite signalling for DFRC: Dedicated probing signal or not?" Sep. 2020. [Online]. Available: https://arxiv.org/abs/2009.03528v1

[23] F. Liu and C. Masouros, "Joint beamforming design for extended target estimation and multiuser communication," in *Proc. IEEE Radar Conf.*, Florence, Italy, 2020, pp. 1–6.

[24] C. Masouros and E. Alsusa, "Dynamic linear precoding for the exploitation of known interference in MIMO broadcast systems," *IEEE Trans. Wireless Commun.*, vol. 8, no. 3, pp. 1396–1404, Mar. 2009.

[25] C. Masouros and G. Zheng, "Exploiting known interference as green signal power for downlink beamforming optimization," *IEEE Trans. Signal Process.*, vol. 63, no. 14, pp. 3628–3640, Jul. 2015.

[26] M. Alodeh *et al.*, "Symbol-level and multicast precoding for multiuser multiantenna downlink: A state-of-art, classification, and challenges," *IEEE Commun. Surv. Tut.*, vol. 20, no. 3, pp. 1733–1757, Jul.–Sep. 2018.

[27] A. Li *et al.*, "A tutorial on interference exploitation via symbol-level precoding: Overview, state-of-the-art and future directions," *IEEE Commun. Surv. Tut.*, vol. 22, no. 2, pp. 796–839, Apr.–Jun. 2020.

[28] R. Liu, M. Li, Q. Liu, and A. L. Swindlehurst, "Joint symbol-level precoding and reflecting designs for IRS-enhanced MU-MISO systems," *IEEE Trans. Wireless Commun.*, vol. 20, no. 2, pp. 798–811, Feb. 2021.

[29] R. Liu, M. Li, Q. Liu, A. L. Swindlehurst, and Q. Wu, "Intelligent reflecting surface based passive information transmission: A symbol-level precoding approach," *IEEE Trans. Veh. Technol.*, vol. 70, no. 7, pp. 6735–6749, Jul. 2021.

[30] R. Liu, H. Li, M. Li, and Q. Liu, "Secure symbol-level precoding design for QAM signals in MU-MISO wiretap systems," in *Proc. IEEE Int. Conf. Commun.*, Dublin, Ireland, 2020, pp. 1–6.

[31] A. Li, C. Masouros, B. Vucetic, Y. Li, and A. L. Swindlehurst, "Interference exploitation precoding for multi-level modulations: Closed-form solutions," *IEEE Trans. Commun.*, vol. 69, no. 1, pp. 291–308, Jan. 2021.

[32] H. Jedda, A. Mezghani, A. L. Swindlehurst, and J. Nossek, "Quantized constant envelope precoding with PSK and QAM signaling," *IEEE Trans. Wireless Commun.*, vol. 17, no. 12, pp. 8022–8034, Dec. 2018.

[33] P. Stoica, J. Li, and Y. Xie, "On probing signal design for MIMO radar," *IEEE Trans. Signal Process.*, vol. 55, no. 8, pp. 4151–4161, Aug. 2007.

[34] S. Sun and A. P. Petropulu, "On transmit beamforming in MIMO radar with matrix completion," in *Proc. IEEE Int. Conf. Acoust. Speech Signal Process.*, Brisbane, Australia, 2015, pp. 2774–2778.

[35] Q. Shi and M. Hong, "Penalty dual decomposition method for nonsmooth nonconvex optimization-Part I: Algorithms and convergence analysis," *IEEE Trans. Signal Process.*, vol. 68, pp. 4108–4122, Jun. 2020, doi: 10.1109/TSP.2020.3001906.

[36] Y. Sun, P. Babu, and D. P. Palomar, "Majorization-minimization algorithms in signal processing, communications, and machine learning," *IEEE Trans. Signal Process.*, vol. 65, no. 3, pp. 794–816, Feb. 2017.

[37] A. Ben-Tal and A. Nemirovski, *Lectures on Modern Convex Optimization: Analysis, Algorithms, and Engineering Applications*. Philadelphia, USA: SIAM, 2001.

[38] R. Liu, M. Li, Q. Liu, and A. L. Swindlehurst, "Secure symbol-level precoding in MU-MISO wiretap systems," *IEEE Trans. Inf. Forensics Secur.*, vol. 15, pp. 3359–3373, Apr. 2020, doi: 10.1109/TIFS.2020.2988127.

[39] V. Torczon, "On the convergence of pattern search algorithms," *SIAM J. Optim.*, vol. 7, no. 1, pp. 1–25, Jan. 1997.

[40] W. Huang, K. A. Gallivan, and P.-A. Absil, "A Broyden class of quasi-Newton methods for Riemannian optimization," *SIAM J. Optim.*, vol. 25, no. 3, pp. 1660–1685, Jan. 2015.

[41] R. Andreani, E. G. Birgin, J. M. Martínez, and M. L. Schuverdt, "On augmented Lagrangian methods with general lower-level constraints," *SIAM J. Optim.*, vol. 18, no. 4, pp. 1286–1309, Nov. 2007.
[42] P.-A. Absil, R. Mahony, and R. Sepulchre, *Optimization Algorithms on Matrix Manifolds*. Princeton, NJ, USA: Princeton Univ. Press, 2009.
[43] L. Xu, J. Li, and P. Stoica, "Target detection and parameter estimation for MIMO radar systems," *IEEE Trans. Aerosp. Electron. Syst.*, vol. 44, no. 3, pp. 927–939, Jul. 2008.

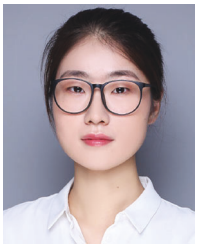

Rang Liu (Graduate Student Member, IEEE) received the B.S. degree in electronics information engineering from the Dalian University of Technology, Dalian, China, in 2018. She is currently studying toward the Ph.D. degree with the School of Information and Communication Engineering, Dalian University of Technology, Dalian, China. Her current research interests include signal processing, massive MIMO systems, reconfigurable intelligent surfaces, and integrated sensing and communication. She was the recipient of the National Scholarship in 2020.

Ming Li (Senior Member, IEEE) received the M.S. and Ph.D. degrees in electrical engineering from the State University of New York at Buffalo (SUNYBuffalo), Buffalo, in 2005 and 2010, respectively. From January 2011 to August 2013, he was a Postdoctoral Research Associate with the Department of Electrical Engineering, SUNY-Buffalo. From August 2013 to June 2014, he joined Qualcomm Technologies Inc. as a Senior Engineer. Since June 2014, he has been with the School of Information and Communication Engineering, Dalian University of Technology, Dalian, China, where he is currently a Professor. His current research interests include the general areas of communication theory and signal processing with applications to intelligent reflecting surface, mmWave communications, massive MIMO systems, and secure wireless communications. He is the Co-Chair for IEEE INFOCOM 2019 workshop on "Wireless Communications and Networking in Extreme Environments."

Qian Liu (Member, IEEE) received the B.S. and M.S. degrees from the Dalian University of Technology, Dalian, China, in 2006 and 2009, respectively, and the Ph.D. degree from The State University of New York at Buffalo (SUNY-Buffalo), Buffalo, NY, USA, in 2013. She was a Postdoctoral Fellow with the Ubiquitous Multimedia Laboratory, SUNY-Buffalo from 2013 to 2015. She received the Alexander von Humboldt Fellowship in 2015, and was a Postdoctoral Fellow with the Chair of Media Technology and the Chair of Communication Networks, Technical University of Munich, from 2016 to 2017. She is currently an Associate Professor with the School of Computer Science and Technology, Dalian University of Technology, China. Her current research interests include multimedia transmission over MIMO systems, IEEE 802.11 wireless networks and LTE networks, device-to-device communication, energy-aware multimedia delivery, and the Tactile Internet. She was the recipient of the the Best Paper Runner-up Award at the 2012 IEEE International Conference on Multimedia and Expo, and was in the finalist for the Best Student Paper Award at the 2011 IEEE International Symposium on Circuits and Systems.

A. Lee Swindlehurst (Fellow, IEEE) received the B.S. and M.S. degrees in electrical engineering from Brigham Young University (BYU), USA, in 1985 and 1986, respectively, and the Ph.D. degree in electrical engineering from Stanford University, USA, in 1991. He was with the Department of Electrical and Computer Engineering, BYU from 1990to 2007, where he was the Department Chair from 2003to 2006. During 1996 to 1997, he held a joint appointment as a Visiting Scholar with Uppsala University and the Royal Institute of Technology in Sweden. From 2006to 2007, he was on leave working as the Vice President of Research for ArrayComm LLC in San Jose, California. Since 2007, he has been a Professor with the Electrical Engineering and Computer Science Department, the University of California Irvine, where he was an Associate Dean for Research and Graduate Studies with the Samueli School of Engineering from 2013 to 2016. During 2014 to 2017, he was also a Hans Fischer Senior Fellow with the Institute for Advanced Studies, the Technical University of Munich. In 2016, he was elected as a Foreign Member of the Royal Swedish Academy of Engineering Sciences (IVA). His research interests include array signal processing for radar, wireless communications, and biomedical applications, and he has more than 300 publications in these areas. Dr. Swindlehurst was the inaugural Editor-in-Chief of the IEEE Journal of Selected Topics in Signal Processing. He was the recipient of the 2000 IEEE W. R. G. Baker Prize Paper Award, the 2006 IEEE Communications Society Stephen O. Rice Prize in the Field of Communication Theory, the 2006 and 2010 IEEE Signal Processing Society's best paper awards, and the 2017 IEEE Signal Processing Society Donald G. Fink Overview Paper Award.